Supporting Information

Activation of caspase-9 on the apoptosome as studied by methyl-TROSY NMR

Materials and Methods

Plasmid constructs and cloning

A codon-optimized version of the human Casp9 gene (residues 1-416, UniProt: P55211) was synthesized by GenScript and subcloned into a *Champion* pET-SUMO vector (kanamycin resistance) with a His_5-SUMO tag. To allow for efficient cleavage of the tag, a Ser-Gly motif (herein referred to as residues -1-0) was introduced immediately following the Ulp1 cut-site (*i.e.*, …REQIGG↓SG…, where ↓ represents the cut-site). All Casp9 mutants utilized in this study were generated via QuikChange site-directed mutagenesis (Agilent) or Gibson Assembly (New England BioLabs Inc.). To produce the Casp9′ construct (Fig. 4A), residues -1-95 of the Casp9 construct were removed and replaced with the SH3-domain of *S. cerevisiae* actin-binding protein (residues 535-592, UniProt: P15891), with an additional Ser-Ala-Met-Ala sequence at the N-terminus (cloning scar). In addition, residues 121-128 (RPETPRP) in the linker region connecting the SH3 domain and the PD were mutated to GFEVKKS to prevent binding of this proline-rich sequence to the SH3 domain. A sequence alignment of Casp9 proteins from the CaspBase (1) showed that the Pro-rich region of human Casp9 is not present in the *D. melanogaster* protein Dronc (UniProt: Q9XYF4). Instead, the corresponding residues in Dronc are ^{167}GPEVKKS^{173}. An additional Pro-to-Phe mutation (P168F in Dronc numbering) was introduced to remove the lone remaining Pro residue, yielding the final GFEVKKS sequence used in Casp9′. The α′ construct (Fig. 4A) was produced by joining the N-terminal 17-residue peptide from *S. cerevisiae*, referred to as Ark1p (residues 605-621, Uniprot: P53974), the 16 amino-acid linker between CARD and the ATPase domain from the human Apaf1 gene (residues 90-105, UniProt: O14727), and the α-subunit of the 20S core particle from the archaeon *Thermoplasma acidophilum* (UniProt: P25156). We have used the gateless α-subunit sequence

with residues 1-12 of the original construct removed. In addition, residues 97–103 of α were eliminated (residues 13-96 joined to residues 104-233) to ensure that only a single heptameric ring structure is formed (2). The final construct was of the form Ark1p-linker-α. The gene was produced by Gibson Assembly and subcloned into a pET His_6-SUMO backbone. To generate the leucine-zipper linked dimeric Casp9 (Casp9 LZ) construct, residues 1-95 of the Casp9 construct were removed and replaced with the leucine-zipper motif of GCN4 (residues 251-281, UniProt: P03069) via Gibson Assembly (3). The human Apaf1 gene (residues 1-1248, UniProt: O14727) with an N-terminal His_6-tag and C-terminal His_9-tag (both non-cleavable) in a pFastBac vector (ampicillin and gentamycin resistance) was obtained from Dr. Christopher Akey (Boston University). The N-terminal His_6-tag was removed via mutagenesis, generating a construct with only a C-terminal His_9-tag. The Abp1p-SH3 and Ark1p plasmids were obtained from previous studies (4). Amino acid sequences of the major constructs are outlined below in *SI Appendix*, Table S1.

E. coli protein expression and purification

For production of unlabeled protein in *E. coli*, transformed BL21(DE3)-RIPL cells were grown in LB medium at 37°C. Once an OD_{600} of ~0.7 was reached, protein expression was induced via addition of 0.2 mM isopropyl β-D-1-thiogalactopyranoside (IPTG) with protein production for ~18 hours at 16°C (Casp9 constructs) or 25°C (α′, Abp1p-SH3, and Ark1p peptide). For production of labeled samples, transformed *E. coli* BL21(DE3)-RIPL cells were grown in minimal M9 medium. Perdeuterated (U-^{2}H) samples were grown in minimal M9 D_2O medium supplemented with d_7-glucose as the sole carbon source. For U-^{2}H samples with ILVM $^{13}CH_3$-labeling (with only one of the pair of isopropyl methyls of Leu and Val $^{13}CH_3$ labeled),

precursors (60 mg/L α-ketobutyric acid, methyl-^{13}C{3,3-D2} for Ileδ1-$^{13}CH_3$; 100 mg/L α-ketoisovaleric acid, 3-methyl-^{13}C{3,4,4,4-D4} for Leuδ,Valγ-$^{13}CH_3/^{12}CD_3$ (5); and 100 mg/L methyl-$^{13}CH_3$-methionine for Metε-$^{13}CH_3$ (6)) were added 1 hour prior to induction of protein overexpression. For production of fully protonated samples with ILVM-labeling, for assignment purposes, where both isopropyl methyls of Leu and Val are $^{13}CH_3$, transformed *E. coli* were grown in minimal M9 H_2O medium and precursors (60 mg/L α-ketobutyric acid, methyl-^{13}C for Ileδ1-$^{13}CH_3$; 100 mg/L α-ketoisovaleric acid, dimethyl-^{13}C for Leuδ,Valγ-$^{13}CH_3/^{13}CH_3$; and 100 mg/L methyl-$^{13}CH_3$-methionine for Metε-$^{13}CH_3$) were added 1 hour prior to induction of protein overexpression. For production of U-^{13}C,^{15}N labeled Casp9 CARD+linker (residues -1-138), minimal M9 H_2O medium was supplemented with uniform-^{13}C-glucose and $^{15}NH_4Cl$ as the sole carbon and nitrogen sources, respectively. Finally, for production of U-^{2}H Casp9 PD F404D with LV-labeling (both isopropyl methyl groups of Leu and Val are $^{13}CH_3$) for ^{13}C-edited NOESY and 3D heteronuclear multiple-bond HMQC (7) experiments, transformed *E. coli* cells were grown in minimal M9 D_2O medium and precursors (100 mg/L α-ketoisovaleric acid, dimethyl-^{13}C for Leuδ,Valγ-$^{13}CH_3/^{13}CH_3$) were added 1 hour before induction of protein overexpression. Prior to addition of precursors, the Leuγ/Valβ-^{12}CH proton was exchanged to Leuγ/Valβ-^{12}CD via incubation in 100% D_2O (pD 12.0) at 45°C for 8 hours. Labeled proteins were produced by incubating transformed cells at 37°C until OD_{600} ~ 0.8, at which point 0.2 mM IPTG was added, and cells were allowed to grow for ~18 hours at 16°C (for U-^{1}H/^{2}H wild-type Casp9 constructs and U-^{1}H C287A Casp9 constructs), ~18 hours at 25°C (for α′), or ~6 hours at 37°C (for U-^{2}H C287A Casp9 and U-^{2}H F404D Casp9 constructs).

Purification of WT Casp9, protonated C287A Casp9, and α′ constructs was achieved by lysing cells in lysis buffer (50 mM Tris, 500 mM NaCl, 20 mM imidazole, 2 mM DTT, 0.1

mg/mL lysozyme, pH 8.0) via sonication, and then centrifugation of lysate at 13,800 x *g* for 20 minutes. The supernatant was loaded directly onto an equilibrated nickel affinity column and contaminants were removed by washing with lysis buffer. The protein of interest was eluted using ~20 mL of elution buffer (50 mM Tris, 100 mM NaCl, 500 mM imidazole, 2 mM DTT, pH 8.0). The eluate was place at 4°C for ~18 hours, and the N-terminal His-SUMO tag was cleaved by the addition of His-tagged Ulp1 protease (8). The cleaved protein was concentrated to ~1-2 mL using a 10kDa MWCO Amicon Ultra-15 concentrator. The concentrated sample was loaded onto a HiLoad 16/600 Superdex 75 PG (Cytiva) size-exclusion chromatography (SEC) column, equilibrated with SEC buffer (50 mM Tris, 100 mM NaCl, pH 8.0) with 5 mM β-mercaptoethanol (BME), and fractions containing the protein of interest were collected. As a final purification step, a second nickel affinity column was run on the SEC fractions in order to remove any residual His-SUMO tag and His-Ulp1.

Purification of U-^{2}H C287A Casp9 was achieved via an inclusion body (IB) method. Cells were lysed in ~25 mL IB buffer (50 mM Tris, 500 mM NaCl, 20 mM DTT, 5mM EDTA, 0.1 mg/mL lysozyme, pH 8.0) + 1% Triton X-100 via sonication, and then centrifuged to pellet IBs. The supernatant was removed, and IBs were then washed once with ~25 mL IB buffer + 500 mM NaCl. The IBs were then resuspended in ~8 mL of 6 M Guanidine-HCl, 100 mM NaH_2PO_4, 500 mM NaCl, 10 mM BME, pH 8.0. Refolded Casp9 was obtained by 10x (*i.e.* ~80 mL) dilution into ice-cold refolding buffer (50 mM Tris, 300 mM NaCl, 500 mM arginine, 10% glycerol, pH 8.0) with rapid stirring. The N-terminal His-SUMO tag was cleaved via addition of Ulp1 protease along with dialysis in ~2 L of 50 mM Tris, 300 mM NaCl, 5 mM BME, pH 8.0 at 4°C for ~18 hours. The cleaved, refolded protein was concentrated to ~2-3 mL using a 10kDa MWCO stir concentrator. The concentrated sample was loaded onto a HiLoad 16/600 Superdex

75 PG (Cytiva) SEC column, equilibrated with SEC buffer with 5 mM BME, and fractions containing the protein of interest were collected. Finally, a second nickel affinity column was run on the SEC fractions to remove any residual His-SUMO tag. Abp1p-SH3 and the Ark1p peptide were purified following a previously described protocol (4). In all cases, purified proteins were buffer exchanged into final buffers used for experiments (as noted in each section below) using Amicon Ultra-15 concentrators. Protein concentrations were measured at 280nm using a NanoDrop Spectrophotometer and their corresponding extinction coefficient (Table S1), established from the ExPASy ProtParam tool (https://web.expasy.org/protparam/protparam-doc.html). The Ark1p peptide concentration was measured via ^{1}H NMR relative to a standard of known concentration.

Apaf1 expression, purification, and assembly

The pFastBac plasmid containing Apaf1 with a C-terminal His_9-tag was transformed into DH10Bac *E. coli* cells. These were plated on LB agar containing 50 μg/mL kanamycin, 7 μg/mL gentamycin, 10 μg/mL tetracycline, along with 100 μg/mL Bluo-Gal and 40μg/mL IPTG (9). After incubation at 37°C for 48 hours, blue-white screening was utilized to select a colony which contained the properly formed bacmid DNA. This bacmid DNA was isolated using a mini-prep kit (Geneaid) and sent to the Baylor College of Medicine Protein and Monoclonal Antibody Production Core (https://www.bcm.edu/research/atc-core-labs/protein-and-monoclonal-antibody-production-core/services/recombinant-protein-expression) where a baculovirus stock was generated for transfection of Sf9 insect cells. To produce unlabeled Apaf1, in brief, Sf9 cells were grown in Grace's Insect Medium supplemented with 10% fetal bovine serum (FBS) using an oxygenated bioreactor. Transfection with a baculovirus harboring the Apaf1 gene was

performed, and then protein expression was allowed to occur for 48 hours at 27°C. The culture was centrifuged at 4°C to pellet cells, and pellets were washed once with phosphate buffered saline. Finally, the Sf9 pellets were flash frozen using liquid nitrogen, and shipped on dry-ice. Upon arrival, pellets were stored at -80°C prior to purification.

All purification and concentrating steps prior to apoptosome assembly took place at 4°C, as monomeric Apaf1 is unstable at room temperature. Sf9 cell pellets were removed from the -80°C freezer and were resuspended in ice-cold Apaf1 lysis buffer (20 mM HEPES, 10 mM KCl, 1.5 mM $MgCl_2$, 1 mM EDTA, 1 mM EGTA, 2 mM DTT, 30 mM imidazole, pH 7.5) (10, 11). Cells were lysed via sonication and then centrifuged at 13,800 x *g* for 15 minutes. The supernatant was loaded onto an equilibrated nickel affinity column and contaminants were removed by washing with 10 column volumes (CV) of Apaf1 lysis buffer containing 1 M NaCl. The His-tagged Apaf1 protein was eluted with 4 CV of Apaf1 lysis buffer containing 500mM imidazole, and the nickel column eluant was concentrated to ~4 mL using a 30 kDa MWCO Amicon Ultra-15 concentrator. This was loaded (4 x 1 mL injections) onto a 10/300 Superose 6 SEC column (Cytiva), equilibrated with SEC buffer that was supplemented with 5mM BME, and the fractions containing Apaf1 monomer were collected. Using a 30 kDa MWCO Amicon Ultra-15 concentrator, the Apaf1 SEC fractions were concentrated to ~1 mL and the absorbance of Apaf1 measured using a NanoDrop Spectrophotometer from which the concentration was calculated based on the 280 nm extinction coefficient listed in Table S1. To assemble the apoptosome, the purified Apaf1 monomer was incubated with 2-fold molar excess of equine cytochrome c (CytC) (BioBasic) and 1 mM ATP at 4°C for ~18 hours (10, 11). Final purification of the assembled apoptosome was achieved using a 10/300 Superose 6 SEC column. Assembled apoptosome was buffer exchanged into a final buffer used for experiments with a 50 kDa

MWCO Amicon Ultra-15 concentrator. The concentration of assembled Apaf1 was obtained using a NanoDrop Spectrophotometer with measurements at 280 nm (200,650 $M^{-1}cm^{-1}$ ($\varepsilon_{Apaf1} + \varepsilon_{CytC}$)) and 410 nm (106 mM cm^{-1}, heme group, (12)), with the average of the two measures used as the final concentration.

SEC and SEC-MALS measurements (Fig. 1C)

Samples of unlabeled WT Casp9 PD and C9toC3 (sequences in *SI Appendix*, Table S1) at a concentration of 200 μM were prepared in analysis buffer (25 mM HEPES, 20 mM TCEP, 70 mM NaCl, pH 8.0, 100% H_2O). To produce a WT Casp9 PD sample that was completely reacted with Z-LEHD-fmk inhibitor (13, 14), a solution of 200 μM WT Casp9 PD was incubated with a 1:1 molar equivalent of inhibitor for 24 hours at 25°C, followed by addition of another equivalent, and incubation for a further 24 hours at 25°C. Size-exclusion chromatography coupled to multi-angle light scattering (SEC-MALS) experiments were performed on an Agilent 1260 Infinity II LC system with a 10/300 Superdex 75 column (Cytiva) for the SEC component of the experiment; the flow from the column was passed to a miniDAWN TREOS (Wyatt) and an Optilab rEX (Wyatt) detector for MALS. The system was equilibrated with SEC Buffer containing 2mM TCEP for ~18 hours at a low flow-rate. Each 100-μL injection contained 200μM of the respective sample. SEC-MALS data analysis was carried out using the ASTRA software suite, allowing for the extraction of molecular weights. In brief, the baseline for each trace was auto-selected and manually checked to ensure a reasonable fit. Then the peak of interest was selected, and normalization, alignment, and band broadening procedures were performed to synchronize the signals from all detectors. The data was then exported and plotted using in-house Python3 (v3.11.1) scripts. For SEC experiments of WT Casp9 FL ± inhibitor, a

similar procedure was followed, with the exception that SEC was performed on an FPLC without MALS.

ITC measurements

i) Determining K_D^{PD} for the Casp9 PD using ITC (Fig. 1D, *SI Appendix* Fig. S2, & *SI Appendix*, Fig. S5)

Concentrated samples of unlabeled WT Casp9 PD (2.63 mM), WT Casp9 FL (1.63 mM), and C287A Casp9 PD (1.66 mM) were prepared and buffer exchanged into analysis buffer. Experiments were performed in triplicate on a MicroCal AutoITC-200 instrument (Malvern Panalytical) at 25°C. The injection syringe was loaded with 40 μL of the respective Casp9 stock solution which was subsequently injected step-wise into a 200-μL cell containing only analysis buffer. Each experiment consisted of an initial 'dummy injection' of 0.2 μL, followed by 14 injections of 2.8 μL, with 300 s in-between to allow the system to return to equilibrium.

The released heats for each injection were extracted using the Origin software package and were exported for further analysis using an in-house Python3 script. Subsequently, the ITC dilution data, excluding the 'dummy injection', were fit analytically to a dimer-monomer dissociation ($M_2 \rightleftharpoons M + M$) model as described previously (15). Briefly, the total concentration of macromolecule in the cell after the i^{th} injection, $M_{T,i}$, is given by

$$M_{T,i} = M_0 \cdot \left(1 - \left(1 - \frac{v}{V}\right)^i\right) \quad [S1]$$

where M_0 is the concentration of macromolecule in the syringe, v is the injection volume, and V is the total volume of the cell. This can be used to calculate the monomer concentration of the macromolecule after the i^{th} injection, M_i

$$M_i = \frac{K_D}{4} \cdot \left(\sqrt{1 + \frac{8 \cdot M_{T,i}}{K_D}} - 1 \right) \quad [S2]$$

where K_D is the fitted dissociation constant. To relate these concentration values to the measured experimental heats the theoretical heat released from the i^{th} injection, q_i, is calculated given the molar enthalpy, ΔH_D, of the dissociation reaction, yielding:

$$q_i = V \cdot \Delta H_D \cdot \left(M_i - M_{i-1} \cdot \left(1 - \frac{v}{V} \right) - F_0 \cdot M_0 \cdot \frac{v}{V} \right) \quad [S3]$$

where F_0 is the fraction of monomer in the syringe,

$$F_0 = \frac{K_D}{4 \cdot M_0} \cdot \left(\sqrt{1 + \frac{8 \cdot M_0}{K_D}} - 1 \right). \quad [S4]$$

Using this system of equations (Eq. [S1]-[S4]), the dimer-monomer dissociation constant (K_D) and enthalpy of dissociation (ΔH_D) were obtained via a least-squares fitting approach with an in-house Python3 script.

ii) Determining K_D for the Abp1p-Ark1p interaction by ITC, $K_D^{Ark-SH3}$ (*SI Appendix*, Fig. S8)

Samples of unlabeled Abp1p-SH3 and Ark1p peptide were prepared and exchanged into analysis buffer. As for the ITC dilution experiment described immediately above, measurements were performed in triplicate on a MicroCal AutoITC-200 instrument at 25°C. The injection syringe was loaded with 40 µL of 240 µM Ark1p peptide, and aliquots added step-wise into a 200-µL cell containing 25 µM Abp1p-SH3. Each experiment consisted of a first 'dummy injection' of 0.2 µL, followed by 16 injections of 2.45 µL, with 400 s in-between to allow for the system to return to equilibrium.

The released heats for each injection were extracted using the Origin software package and were exported for further analysis. Using an in-house Python3 script, the ITC association data was fit analytically to an *n*-sites non-cooperative protein+ligand ($P + nL \rightleftharpoons PL_n$) model (15). Briefly, the total concentration of protein, $P_{T,i}$, in the cell after the i^{th} injection is given by

$$P_{T,i} = P_0 \cdot \left(1 - \frac{v}{V}\right)^i \quad [S5]$$

where P_0 is the initial concentration of protein (*i.e.*, Abp1p-SH3) in the cell. In addition, the total concentration of ligand, $L_{T,i}$, in the cell after the i^{th} injection is

$$L_{T,i} = L_0 \cdot \left(1 - \left(1 - \frac{v}{V}\right)^i\right) \quad [S6]$$

where L_0 is the initial concentration of ligand (*i.e.*, Ark1p peptide) in the syringe. Using these values, the amount of complex (PL_n) can be calculated after the i^{th} injection as,

$$PL_{n,i} = \frac{1 + n \cdot P_{T,i} \cdot K_A + K_A \cdot L_{T,i} - \sqrt{\left(1 + n \cdot P_{T,i} \cdot K_A + K_A \cdot L_{T,i}\right)^2 - 4n \cdot P_{T,i} \cdot K_A^2 \cdot L_{T,i}}}{2K_A} \quad [S7]$$

where K_A is the protein+ligand association constant. Finally, the heat released per i^{th} injection, q_i, is calculated from the molar enthalpy, ΔH_A, of the association reaction, yielding:

$$q_i = V \cdot \Delta H_A \cdot \left(PL_{n,i} - PL_{n,i-1} \cdot \left(1 - \frac{v}{V}\right)\right) \quad [S8]$$

Values of $K_A = 1/K_D^{Ark-SH3}$, the molar enthalpy of association (ΔH_A), and the stoichiometry of the interaction (n) are obtained from a fit of the experimental heat profile using a least-squares approach.

NMR measurements

All NMR measurements were acquired at either 23.5 Tesla (1 GHz ^{1}H frequency Bruker Avance NEO), 18.8 Tesla (800 MHz Bruker Avance III HD), or 14.1 Tesla (600 MHz Bruker Avance III HD) at 25°C, using spectrometers equipped with cryogenically cooled x, y, z pulsed-field gradient triple-resonance probes. Unless otherwise specified, samples were in an NMR buffer composed of 25 mM HEPES, 20 mM TCEP, 70 mM NaCl, pD 8.0, 100% D_2O, where pD is the value measured on a pH meter plus 0.4. NMR data were processed using the NMRPipe suite of programs (16) and visualized using the Python3 nmrglue package (https://www.nmrglue.com/). Peak volumes were extracted with an in-house Python3 'box-sum' integration script.

i) Methyl Group Assignments (Fig. 2A, *SI Appendix*, Fig. S3, & *SI Appendix*, Fig. S7)

Methyl assignments of full-length Casp9 were obtained by a 'divide and conquer' approach whereby separate samples of PD and CARD+linker domains were produced and assigned separately. A U-^{13}C,^{15}N sample of the CARD+linker construct was generated (300 μM in protein dissolved in a 25 mM MES, 40 mM NaCl, 5 mM TCEP, 0.5 mM EDTA, pH 5.5, 3% D_2O / 97% H_2O buffer). Backbone and subsequently methyl sidechain assignments were obtained by recording a suite of triple-resonance experiments (HNCO, HN(CA)CO, HNCACB, CBCA(CO)NH, HNN, C(CO)NH, and H(CCO)NH) at 14.1 T, 25 ^{o}C (17, 18). In addition, a long-range ^{13}C-^{13}C J-correlation experiment was recorded to assign the methyl group of Met residues (19). All experiments utilized non-uniform sampling (NUS) with a Poisson-Gap sampling schedule (20), with sampling densities of between 20-30%. NUS-acquired datasets were reconstructed using the SMILE program in NMRPipe (21).

Residues in the substrate-free, monomeric form of the Casp9 PD were assigned via a combined approach, utilizing mutagenesis, 3D heteronuclear multiple-bond HMQC (7) and ^{13}C-edited NOESY experiments (300 ms and 500 ms mixing times). The latter experiments were recorded on a deuterated LV-labeled Casp9 PD F404D sample (both prochiral methyl groups of Leu and Val are $^{13}CH_3$). An AlphaFold2 (22, 23) structural model of the PD was utilized to rationalize NOEs, as there is no high-resolution structure of monomeric Casp9 PD without substrate. Instead, the available X-ray structures of Casp9 PD contain a cleaved p20-p10 linker with an active-site inhibitor bound covalently (PDB ID: 1JXQ (24)), a mutated dimer interface (C9toC3, PDB ID: 2AR9 (25)) to facilitate dimerization, or are bound to other proteins (PDB IDs: 3V3K, 1NW9 (26)). NOESY experiments utilized $^{13}C(t_1)$-NOE-$^{13}C(t_2)$-$^{1}H(t_3)$ and $^{1}H(t_1)$-$^{13}C(t_2)$-NOE-$^{1}H(t_3)$ pulse sequences. In total 19/19 Ile, 56/98 Leu, 22/50 Val, 7/7 Met were assigned in FL Casp9 (see text).

ii) Fitting NMR data

a) Determining K_D^{PD} for the C287A Casp9 PD ($K_D^{PD,C287A}$) using NMR (Fig. 3)

Consider the dimerization reaction $2Y \rightleftharpoons Z_2$ where *Y* is the C287A Casp9 PD monomer and Z_2 is the dimeric form, with a dissociation constant of K_D^{PD}. Then it follows directly that

$$[Y] = \frac{-K_D^{PD} + \sqrt{(K_D^{PD})^2 + 8K_D^{PD}P_T}}{4} \qquad [S9]$$

where $P_T = [Y] + 2[Z_2]$ is the total protein concentration. The values of $Frac_{m_i}^{calc} = \frac{[Y]}{[Y]+2[Z_2]}$ for each residue and for each titration point (i=1,...,N) are calculated (from an initial guess of K_D^{PD}) and then the residual sum-of-squared (RSS) differences between $Frac_{m_i}^{calc}$ and $Frac_{m_i}^{expt}$ (calculated as in Fig. 3B) minimized

$$RSS = \sum_{i=1}^{N} [Frac_{m_i}^{expt}(P_{T,i}) - Frac_{m_i}^{calc}(P_{T,i}, K_D^{PD})]^2 \quad [S10]$$

using the Levenberg-Marquardt algorithm of the LMFIT (v1.2.0) Python software package (https://lmfit.github.io/lmfit-py/).

b) Fitting the $Casp9'$: α' titration data (Fig. 5C)

We have fit the titration data of Figure 5 to the model highlighted in *SI Appendix*, Figure S12A. In the discussion that follows we refer to α' as **X**, a molecule of C287A $Casp9'$ in the monomeric state as **Y**, with **Z** denoting each molecule of C287A $Casp9'$ in the dimeric state. We will distinguish between a free and α' bound molecule of Y using the notation **Y** and $\mathbf{X_7Y}$, respectively, or a pair of free and scaffold bound molecules in the dimeric state as $\mathbf{Z_2}$ (no scaffold) and $\mathbf{X_7Z_2}$ (scaffold). For example, the state depicted at the top-left in *SI Appendix*, Figure S12A is $\mathbf{X_7}$, while the conformer at the bottom-right is $\mathbf{X_7YZ_6}$ where one bound $Casp9'$ is monomeric and the other six form three dimers. The concentrations for the 22 species of interest (illustrated in *SI Appendix*, Fig. S12A) can be calculated, as described below.

Following the model of *SI Appendix*, Figure S12A and including mass conservation (Eqs. [S11]-[S12]), relations for $Casp9'$ - α' binding (Eqs. [S13]-[S28]), and taking into account the $Casp9'$ monomer-dimer equilibrium when free and bound to the scaffold (Eqs. [S29]-[S41]) we obtain:

$$[\alpha']_{\text{TOTAL}} = 7 \cdot ([\mathbf{X_7}] + [\mathbf{X_7Y}] + [\mathbf{X_7Y_2}] + [\mathbf{X_7Y_3}] + [\mathbf{X_7Y_4}] + [\mathbf{X_7Y_5}] + [\mathbf{X_7Y_6}] + [\mathbf{X_7Y_7}] + [\mathbf{X_7Z_2}] + [\mathbf{X_7YZ_2}] + [\mathbf{X_7Y_2Z_2}] + [\mathbf{X_7Y_3Z_2}] + [\mathbf{X_7Y_4Z_2}] + [\mathbf{X_7Y_5Z_2}] + [\mathbf{X_7Z_4}] + [\mathbf{X_7YZ_4}] + [\mathbf{X_7Y_2Z_4}] + [\mathbf{X_7Y_3Z_4}] + [\mathbf{X_7Z_6}] + [\mathbf{X_7YZ_6}]) \quad [S11]$$

$[Casp9']_{\mathrm{TOTAL}}$ = **[Y]** + **[X$_7$Y]** + 2 · (**[Z$_2$]** + **[X$_7$Y$_2$]** + **[X$_7$Z$_2$]**) + 3 · (**[X$_7$Y$_3$]** + **[X$_7$YZ$_2$]**) + 4 · (**[X$_7$Y$_4$]** + **[X$_7$Y$_2$Z$_2$]** + **[X$_7$Z$_4$]**) + 5 · (**[X$_7$Y$_5$]** + **[X$_7$Y$_3$Z$_2$]** + **[X$_7$YZ$_4$]**) + 6 · (**[X$_7$Y$_6$]** + **[X$_7$Y$_4$Z$_2$]** + **[X$_7$Y$_2$Z$_4$]** + **[X$_7$Z$_6$]**) + 7 · (**[X$_7$Y$_7$]** + **[X$_7$Y$_5$Z$_2$]** + **[X$_7$Y$_3$Z$_4$]** + **[X$_7$YZ$_6$]**) [S12]

where $[\alpha']_{\mathrm{TOTAL}}$ is the concentration of α' for each titration point, and $[Casp9']_{\mathrm{TOTAL}}$ = 25 μM which is kept constant for all titration points.

[X$_7$] · **[Y]** / **[X$_7$Y]** = $K_D^{Ark-SH3}$ / 7 [S13]

[X$_7$Y] · **[Y]** / **[X$_7$Y$_2$]** = $K_D^{Ark-SH3}$ / 3 [S14]

[X$_7$Y$_2$] · **[Y]** / **[X$_7$Y$_3$]** = $K_D^{Ark-SH3}$ · 3 / 5 [S15]

[X$_7$Y$_3$] · **[Y]** / **[X$_7$Y$_4$]** = $K_D^{Ark-SH3}$ [S16]

[X$_7$Y$_4$] · **[Y]** / **[X$_7$Y$_5$]** = $K_D^{Ark-SH3}$ · 5 / 3 [S17]

[X$_7$Y$_5$] · **[Y]** / **[X$_7$Y$_6$]** = $K_D^{Ark-SH3}$ · 3 [S18]

[X$_7$Y$_6$] · **[Y]** / **[X$_7$Y$_7$]** = $K_D^{Ark-SH3}$ · 7 [S19]

[X$_7$Z$_2$] · **[Y]** / **[X$_7$YZ$_2$]** = $K_D^{Ark-SH3}$ / 5 [S20]

[X$_7$YZ$_2$] · **[Y]** / **[X$_7$Y$_2$Z$_2$]** = $K_D^{Ark-SH3}$ / 2 [S21]

[X$_7$Y$_2$Z$_2$] · **[Y]** / **[X$_7$Y$_3$Z$_2$]** = $K_D^{Ark-SH3}$ [S22]

[X$_7$Y$_3$Z$_2$] · **[Y]** / **[X$_7$Y$_4$Z$_2$]** = $K_D^{Ark-SH3}$ · 2 [S23]

[X$_7$Y$_4$Z$_2$] · **[Y]** / **[X$_7$Y$_5$Z$_2$]** = $K_D^{Ark-SH3}$ · 5 [S24]

[X$_7$Z$_4$] · **[Y]** / **[X$_7$YZ$_4$]** = $K_D^{Ark-SH3}$ / 3 [S25]

$[\mathbf{X_7YZ_4}] \cdot [\mathbf{Y}] / [\mathbf{X_7Y_2Z_4}] = K_D^{Ark-SH3}$ [S26]

$[\mathbf{X_7Y_2Z_4}] \cdot [\mathbf{Y}] / [\mathbf{X_7Y_3Z_4}] = K_D^{Ark-SH3} \cdot 3$ [S27]

$[\mathbf{X_7Z_6}] \cdot [\mathbf{Y}] / [\mathbf{X_7YZ_6}] = K_D^{Ark-SH3}$ [S28]

$[\mathbf{X_7Y_2}] / [\mathbf{X_7Z_2}] = K_{D,uni}$ [S29]

$[\mathbf{X_7Y_3}] / [\mathbf{X_7YZ_2}] = K_{D,uni} / 3$ [S30]

$[\mathbf{X_7Y_4}] / [\mathbf{X_7Y_2Z_2}] = K_{D,uni} / 6$ [S31]

$[\mathbf{X_7Y_5}] / [\mathbf{X_7Y_3Z_2}] = K_{D,uni} / 10$ [S32]

$[\mathbf{X_7Y_6}] / [\mathbf{X_7Y_4Z_2}] = K_{D,uni} / 15$ [S33]

$[\mathbf{X_7Y_7}] / [\mathbf{X_7Y_5Z_2}] = K_{D,uni} / 21$ [S34]

$[\mathbf{X_7Y_2Z_2}] / [\mathbf{X_7Z_4}] = K_{D,uni} \cdot 2$ [S35]

$[\mathbf{X_7Y_3Z_2}] / [\mathbf{X_7YZ_4}] = K_{D,uni} \cdot 2 / 3$ [S36]

$[\mathbf{X_7Y_4Z_2}] / [\mathbf{X_7Y_2Z_4}] = K_{D,uni} / 3$ [S37]

$[\mathbf{X_7Y_5Z_2}] / [\mathbf{X_7Y_3Z_4}] = K_{D,uni} / 5$ [S38]

$[\mathbf{X_7Y_2Z_4}] / [\mathbf{X_7Z_6}] = K_{D,uni} \cdot 3$ [S39]

$[\mathbf{X_7Y_3Z_4}] / [\mathbf{X_7YZ_6}] = K_{D,uni}$ [S40]

$[\mathbf{Y}]^2 / [\mathbf{Z_2}] = K_D^{Casp9',C287A}$ [S41]

Some of the equations listed above are redundant; only equations ([S11]-[S29]), ([S35]), ([S39] and [S41]) are needed. The remaining equations are not required because the model is comprised of a number of thermodynamic cycles that simplifies the description of the binding, such as:

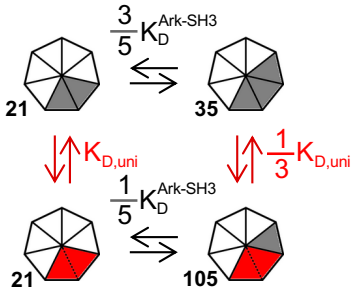

Although each of these cycles is described in terms of four equilibrium constants, only three are required as the fourth can be derived from the first three by requiring that the sum of ΔG values for the complete cycle is zero. Subsequently, the fractions of $Casp9'$ in a monomeric ($Frac_M$) or dimeric conformation ($Frac_D$) were calculated as:

$$Frac_M = (1 \cdot ([\mathbf{Y}] + [\mathbf{X_7Y}] + [\mathbf{X_7YZ_2}] + [\mathbf{X_7YZ_4}] + [\mathbf{X_7YZ_6}]) + 2 \cdot ([\mathbf{X_7Y_2}] + [\mathbf{X_7Y_2Z_2}] + [\mathbf{X_7Y_2Z_4}]) + 3 \cdot ([\mathbf{X_7Y_3}] + [\mathbf{X_7Y_3Z_2}] + [\mathbf{X_7Y_3Z_4}]) + 4 \cdot ([\mathbf{X_7Y_4}] + [\mathbf{X_7Y_4Z_2}]) + 5 \cdot ([\mathbf{X_7Y_5}] + [\mathbf{X_7Y_5Z_2}]) + 6 \cdot ([\mathbf{X_7Y_6}]) + 7 \cdot ([\mathbf{X_7Y_7}])) / [Casp9']_{\mathrm{TOTAL}} \quad [S42]$$

$$Frac_D = (2 \cdot ([\mathbf{Z_2}] + [\mathbf{X_7Z_2}] + [\mathbf{X_7YZ_2}] + [\mathbf{X_7Y_2Z_2}] + [\mathbf{X_7Y_3Z_2}] + [\mathbf{X_7Y_4Z_2}] + [\mathbf{X_7Y_5Z_2}]) + 4 \cdot ([\mathbf{X_7Z_4}] + [\mathbf{X_7YZ_4}] + [\mathbf{X_7Y_2Z_4}] + [\mathbf{X_7Y_3Z_4}]) + 6 \cdot ([\mathbf{X_7Z_6}] + [\mathbf{X_7YZ_6}])) / [Casp9']_{\mathrm{TOTAL}} \quad [S43]$$

with $Frac_M$ and $Frac_D$ defined for each of I154, M212, V231, and L380 as described in the text and in Figure 5C, bottom.

Per-residue values for $K_{D,uni}$ were obtained using a nested minimization routine in which the experimental $Frac_M$ values were compared to the corresponding calculated values. Briefly,

this was accomplished according to the following scheme which involves a pair of minimization steps. In the first minimization, input values for $K_D^{Ark-SH3}$ (the dissociation constant of $Casp9'$ from α'; $K_D^{Ark-SH3}$ = 0.5 μM, see text), $K_D^{Casp9',C287A}$ (the dissociation constant for the FL C287A $Casp9'$ dimer, free in solution; $K_D^{Casp9',C287A}$= 213±72 μM; *SI Appendix*, Fig. S11), $[\alpha']_{\text{TOTAL}}$, $[Casp9']_{\text{TOTAL}}$, along with initial guesses for $K_{D,uni}$ and concentrations of all states were input, from which better estimates of the concentrations (*SI Appendix*, Fig. S12A) were determined using the root-finding algorithm, *scipy.optimize.fsolve* in Python's SciPy (v1.10.1) library. These concentrations were then used to calculate $Frac_M$ as reported by each methyl group, $Frac_{M_i}^{calc}(C_T, L_{T,i}, \zeta)$, that were subsequently compared to the corresponding experimental values via,

$$RSS = \sum_{i=1}^{N} [Frac_{M_i}^{expt}(C_{T,i}, L_T) - Frac_{M_i}^{calc}(C_{T,i}, L_T, \zeta)]^2 \quad [S44]$$

where RSS is minimzed using the Levenberg-Marquardt algorithm of the LMFIT Python software package. In Eq. [S44], $C_{T,i} = [\alpha']_{\text{TOTAL},i}$, $L_T = [Casp9']_{\text{TOTAL}}$, ζ is the collection of parameters that are necessary for the computation of $Frac_M$ and the summation is over all titration points (i). The value of $K_{D,uni}$ was incremented and the minimization returned to the first step to calculate 'better' estimates of the concentrations of the states until a minimum in *RSS* was reached.

c) Estimating the effective concentration of C287A Casp9 bound to the apoptosome (Fig. 6E)

Tethering of Casp9 to a scaffold such as α_7' or the apoptosome increases its propensity to dimerize by a proximity-induced effect. We first asked what the relative fraction of monomer to

dimer is for C287A Casp9 bound to the apoptosome, quantified as $K_{D,uni}$. This was estimated based on an analysis of peak intensities in the spectrum of Figure 6E (right panel) recorded on a sample of 20 μM U-^{2}H, ILVM-labeled WT Casp9 in presence of 40 μM Apaf1. In the analysis below we assume that (i) all added Casp9 is bound to the scaffold, and (ii) equal mixtures of apoptosomes with either three or four bound Casp9 molecules, given the established 4:7 ratio of Casp9:Apaf1 on a single apoptosome (27). Following the derivation given above for the titration of $Casp9'$ with α'_7 we obtain:

$$[\text{Apaf1}]_{\text{TOTAL}} = 7 \cdot ([\mathbf{X_7Y_3}] + [\mathbf{X_7Y_4}] + [\mathbf{X_7YZ_2}] + [\mathbf{X_7Y_2Z_2}] + [\mathbf{X_7Z_4}]) \quad \text{[S45]}$$

$$[\text{Casp9}]_{\text{TOTAL}} = 3 \cdot ([\mathbf{X_7Y_3}] + [\mathbf{X_7YZ_2}]) + 4 \cdot ([\mathbf{X_7Y_4}] + [\mathbf{X_7Y_2Z_2}] + [\mathbf{X_7Z_4}]) \quad \text{[S46]}$$

and

$$[\mathbf{X_7Y_3}] / [\mathbf{X_7YZ_2}] = K_{D,uni} / 3 \quad \text{[S47]}$$

$$[\mathbf{X_7Y_4}] / [\mathbf{X_7Y_2Z_2}] = K_{D,uni} / 6 \quad \text{[S48]}$$

$$[\mathbf{X_7Y_2Z_2}] / [\mathbf{X_7Z_4}] = K_{D,uni} \cdot 2 \quad \text{[S49]}$$

where **X** = Apaf1, and Casp9 in the bound monomeric (dimeric) state is **Y** (**Z**). Defining the fractions of Casp9 in a monomeric or dimeric conformation we obtain:

$$Frac_M = ([\mathbf{X_7YZ_2}] + 2 \cdot [\mathbf{X_7Y_2Z_2}] + 3 \cdot [\mathbf{X_7Y_3}] + 4 \cdot [\mathbf{X_7Y_4}]) / [Casp9']_{\text{TOTAL}} \quad \text{[S50]}$$

$$Frac_D = (2 \cdot ([\mathbf{X_7YZ_2}] + [\mathbf{X_7Y_2Z_2}]) + 4 \cdot [\mathbf{X_7Z_4}]) / [Casp9']_{\text{TOTAL}} \quad \text{[S51]}$$

Eqs [S45]-[S49] are solved as described above in '*Fitting the $Casp9'$: α' titration data* (Fig. 5)', to the experimentally determined $Frac_D$ = 0.712 yielding $K_{D,uni}$ = 0.31, $[\mathbf{X_7YZ_2}]$ = 2.6 μM,

[$\mathbf{X_7Y_2Z_2}$] = 1.08 μM, [$\mathbf{X_7Y_3}$] = 0.27 μM, [$\mathbf{X_7Y_4}$] = 0.05 μM, [$\mathbf{X_7Z_4}$] = 1.73 μM (the concentrations listed are those of each complex).

We have also considered a second model whereby Casp9 only binds to the apoptosome in a 4:7 ratio. Given the 20 μM Casp9 : 40 μM Apaf1 ratio used, corresponding to a total concentration of apoptosome of 40/7μM = 5.7 μM, 5 μM of scaffold is Casp9 bound (4:7) and 0.7 μM is empty. In this case $K_{D,uni}$ = 0.53, [$\mathbf{X_7Y_2Z_2}$] = 2.46 μM, [$\mathbf{X_7Y_4}$] = 0.22 μM, [$\mathbf{X_7Z_4}$] = 2.33 μM. Note that these parameters are also in agreement with $Frac_D$ = 0.712, as they must be, since they were obtained by minimizing to this value.

We next asked what the concentration of C287A Casp9, free in solution, would have to be to achieve the same level of dimerization as observed when C287A Casp9 is tethered (referred to as the effective Casp9 concentration). Considering the dimerization reaction for untethered C287A Casp9

$$2Y \leftrightharpoons Z_2 \qquad [S52]$$

with the dissociation constant $K_D^{PD,C287A} = \frac{[Y]^2}{[Z_2]}$, it follows that the fraction of dimer is

$$f_{Z_2} = \frac{2[Z_2]}{[Y]+2[Z_2]} = \frac{2[Y]}{K_D^{PD,C287A}+2[Y]}. \qquad [S53]$$

We define $[Y]_{eff}$ as the solution to $f_{Z_2} = Frac_D$, where $Frac_D$ is determined experimentally (Fig. 6E, right panel) or by Eq. [S51] with the values for the concentrations of each of the conformers noted above. Values of $[Y]_{eff}$ = 136 μM and $[Y]_{eff}^T = [Y]_{eff} + 2\frac{[Y]_{eff}^2}{K_D^{PD,C287A}}$ = 474 μM ($K_D^{PD,C287A}$= 110 μM) are obtained. Thus, the effective total concentration of (untethered) C287A Casp9 PD that is required to obtain the same dimer concentration as observed on the apoptosome is 474 μM. For $[Y]_{eff}^T$ = 474 μM, the effective monomer and dimer concentrations are $[Y]_{eff}$=

136 μM, and $[Z_2]_{eff} = 169$ μM, respectively. Finally, it is important to note that effective total concentration is model independent. This is because $[Y]^T_{eff}$ is obtained directly from Eq. [S53] where f_{Z_2} is a measured parameter. In contrast, $K_{D,uni}$ is model dependent because different models can accomodate different numbers of dimers. For example, Model 1 above requires 50% apoptosomes with three Casp9, which can form at most one dimeric Casp9, and 50% apoptosomes with four Casp9, potentially forming two dimers. In contrast, when all of the bound apoptosomes have four Casp9 (Model 2 above) there is the potential for a larger fraction of dimers. As the fraction of Casp9 dimers is a fixed parameter determined by experiment, however, the fitted $K_{D,uni}$ adjusts to ensure that the experimental value is realized.

Effect of assumption of equal volumes for I154 and M212 dimer peaks, D1=D2 (Fig. 3B and Fig. 6)

One of the two dimer peaks for both I154 and M212 (labeled as D2 in Fig. 3B) overlaps with the correpsonding monomer peak, complicating extraction of $Frac_D$ and $Frac_M$ that are subsequently fit to obtain $K_D^{PD,C287A}$ (see Fig. 3B). The analysis of the data in the paper is based on the assumption that the volumes of each of the dimer peaks are equal (D1=D2). In an effort to evaluate the validity of this assumption we turn to a 2D ^{1}H-^{13}C HMQC spectrum of U-^{2}H, ILVM-labeled WT Casp9 PD in the presence of excess inhibitor, Z-LEHD-fmk (88 μM Casp9, 400 μM inhibitor) recorded at 14.1 T, 25 ^{o}C. An incubation period of 18 h preceded recording of the dataset to ensure that all of the Casp9 had reacted so that only dimer peaks would be visible in the spectrum. This is in contrast to the C287A dimer that was used in some of the analyses where the weak dimer association ensures that both monomer and dimer correlations are present in spectra, even at relatively high concentrations of Casp9 (as in Fig. 3B, for example). The

dimer peaks of the Casp9-inhibitor complex were fit using the *nlinLS* program from *NMRPipe* (16) as well as *Peakipy* (https://github.com/j-brady/peakipy), both of which calculate volumes of individual peaks in a cluster. Indentical values for the volumes of peaks D1 and D2 were obtained using both programs, with D2/D1 = 1.09±0.01 and 1.08±0.02 for I154 and M212, respectively (*SI Appendix*, Fig. S4). Using a ratio of D2/D1 = 1.1 (rather than 1.0) has a small effect on $K_D^{PD,C287A}$ values, with a change from 105 μM and 107 μM (D2/D1 = 1) to 88 μM and 89 μM, for I154 and M212, respectively. Further, the effective concentration of Casp9 protease domains on the surface of the apoptosome, as estimated from the fraction of dimer calculated from monomer and dimer peak intensities of I154 (Fig. 6E), changes from 470 μM (assuming D2/D1 =1) to 560 μM (D2/D1 = 1.1). Because the changes are small, and have no effect on any of the conclusions, we have assumed D2/D1 = 1 in the analysis of all data for I154 and M212 throughout the manuscript.

Fluorescent assays (Fig. 4D and Fig. 6B)

The protease activity of Casp9 was measured at 25°C using the peptide Ac-LEHD-AMC (Enzo Life Sciences) as a substrate, where a fluorogenic 7-Amino-4-methylcoumarin (AMC) group was covalently attached to the C-terminus and the N-terminus was acetylated. All fluorescent assays utilized a Synergy Neo2 96-well microplate reader, with measurements at 1-minute intervals using λ_{ex}: 355nm and λ_{em}: 460nm with 10-nm bandwidths. Assays were conducted in analysis buffer with 1 μM Casp9, 200 μM substrate peptide, and any additional components (*i.e.*, α′, apoptosome) as described in the main text. Substrate cleavage rates were obtained from initial rates extracted using an in-house Python3 script. All assay conditions were performed in triplicate, and error bars representing one standard deviation are illustrated.

Calculating the volume accessible to bound Casp9 on the apoptosome (*SI Appendix*, Fig. S13)

Our goal is to calculate the volume that is available to the PDs that are tethered to the four Casp9 molecules bound to the apoptosome, from which the effective PD concentration can be obtained. Recall that the linker and PD for each attached Casp9 were not observed in the cryo-EM structures (PDB IDs: 5JUY (10), 5WVE (11)), so that the effective volume occupied by the PDs can only be obtained indirectly. Starting from the cryo-EM structure of the apoptosome (PDB ID: 5WVE) all non-protein components (for example, ions) were removed, along with two Apaf1 CARDs bound to one Casp9 CARD that was not localized to the center of the structure. Thus, the starting structure was comprised of the apoptosome scaffold containing the four central Apaf1 CARD domains to which were attached Casp9 CARD domains in the cryo-EM map. Note that including Apaf1 CARD domains that are not in the periphery of the structure or are not bound to Casp9 CARD makes little difference to the resulting calculated volume.

To generate the volume accessible to Casp9 PDs, we begin by producing all-atom conformations of the intrinsically disordered regions (IDRs) between the CARD and PD (residues 97-149) using IDPConformerGenerator (28, 29). These IDRs were then attached to the AlphaFold2-predicted structure of Casp9 residues 150-416 within the PD region that are well-ordered, forming unique linker+PD conformations (residues 97-416). Resulting structures with clashes between the attached linker and PD were removed. The resulting linker+PD structures were subsequently attached onto residues 1-96 of each of the four target Casp9 CARD domains in the starting cryo-EM structure, and any of the resulting structures with clashes removed. Each of the four PDs from a clash-free apoptosome generated in this step was then saved.

We define a pose as a complete structure with all four full-length Casp9 molecules bound

to the apoptosome. For example, as there are four PDs per pose, 25 poses would correspond to 100 total PDs sampled in space. We considered different numbers of poses, *N*, $N \in \{25 - 5000\}$ by combining the 4*N* PDBs of the 4*N* PDs of the *N* poses. UCSF ChimeraX (30, 31) was used to calculate the resulting surface area and volume of the mesh defined by the poses as a function of *N* (*SI Appendix*, Fig. S13). The local concentration (in mol/L) of the PDs was then obtained from the relation $\frac{4}{N_A \times V}$, where N_A is Avogadro's number, V is the volume calculated (in L), and the factor of 4 is the number of Casp9 molecules tethered to the central disk.

It is important to emphasize that, in principle, the volume available to the PDs of the four apoptosome-attached Casp9 molecules could have been calculated from the appropriate molecular dynamics trajectory with sufficient sampling to ensure that all accessible regions of space are explored. In our hands we have found this approach to be inefficient and have, therefore, chosen the procedure outlined above, where we generate *N* poses and superimpose all *N* poses to obtain the total volume accessible to the PDs. Of course, only four Casp9 molecules are bound at a given time, but the superposition of many poses 'traces out' the volume that is accessible to these four molecules over time. For a superposition of a small number of poses (before convergence) the volume traced out will not represent the complete space accessible to the PDs, giving rise to artificially high concentrations. Only, when the volume does not change with *N* has the total accessible volume been sampled.

Supporting Information Figures

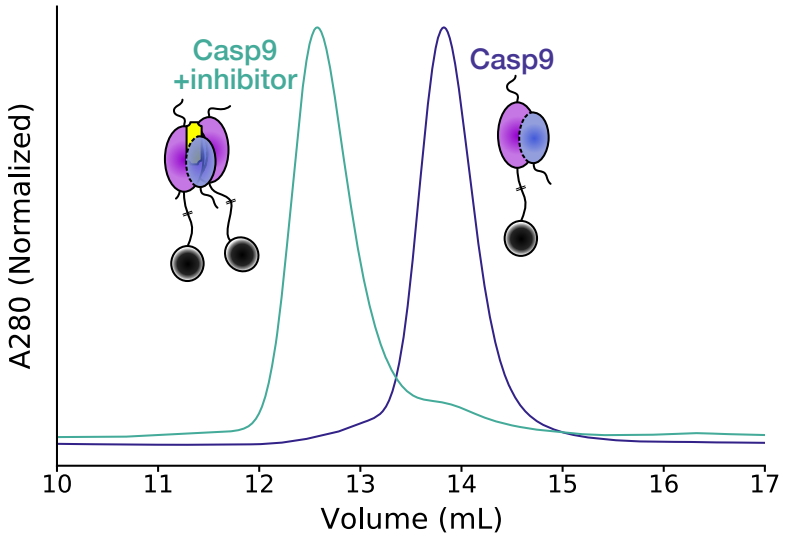

Figure S1. SEC profiles of WT Casp9 FL in the absence (navy) and presence of the substrate mimic 'inhibitor' Z-LEHD-fmk (turquoise). The dimerization behaviour of the FL construct mimics that of the PD (see Fig. 1C). Note that a different size-exclusion column (Cytiva 10/300 Superdex 200 Increase GL) was used to generate these profiles from the one used in Figure 1C.

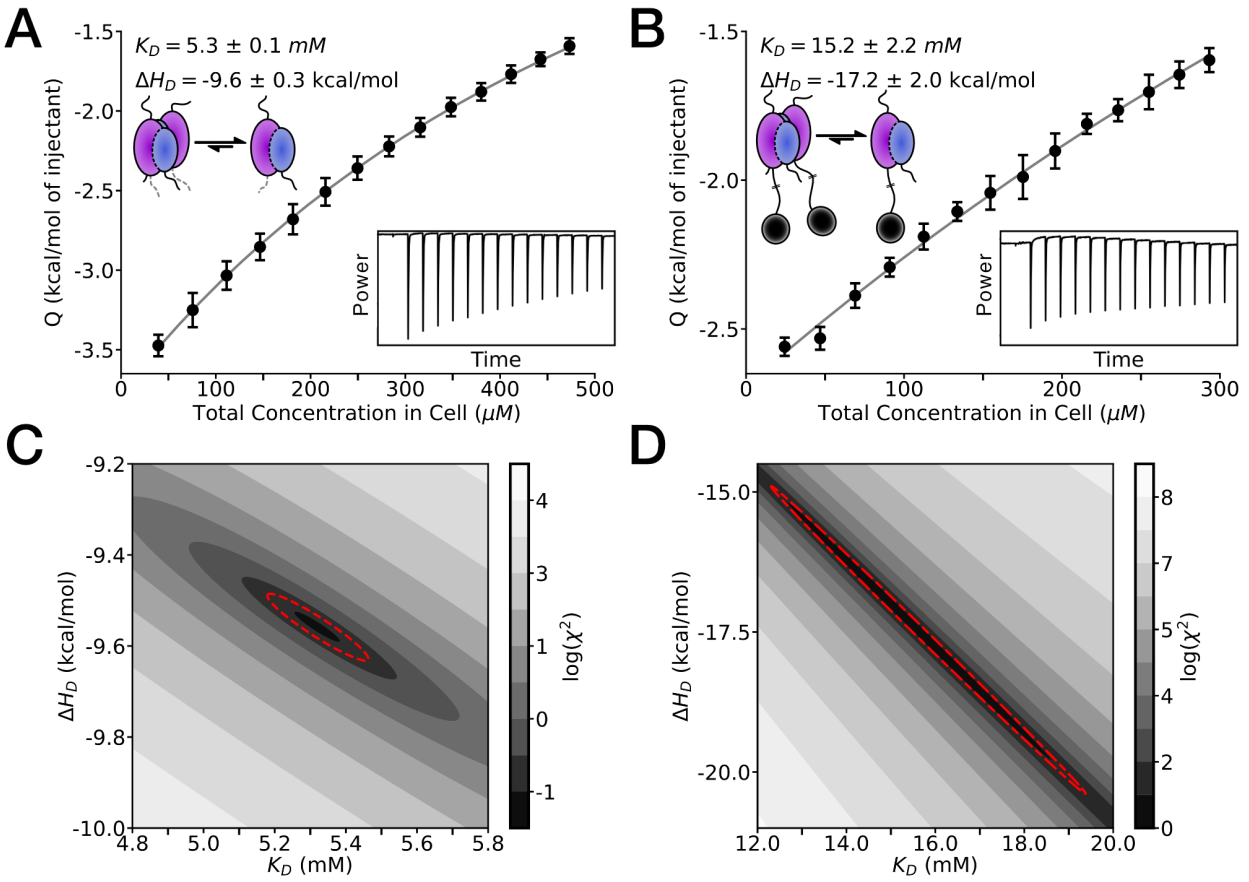

Figure S2. ITC profiles of WT Casp9 (**A**) PD and (**B**) FL at 25°C. The experimental heats (black circles) were fit (solid line) to a monomer-dimer dissociation model ($M + M \rightleftharpoons M_2$), and K_D and ΔH_D values were extracted. Raw thermograms are shown in the insets. To assess the robustness of the fitted parameters in (A) and (B), chi-squared (χ^2) surface plots were constructed and shown in (C) and (D), respectively. These were generated by calculating a χ^2 value for all combinations of the fitted parameters, K_D and ΔH_D. Plots of the χ^2-surface reveal the extent of correlation between K_D and ΔH_D (in these cases they are anti-correlated). Parameter errors can be estimated from the range of parameter values at the 95% confidence levels (dotted red lines) and are consistent with those obtained from triplicate measurements.

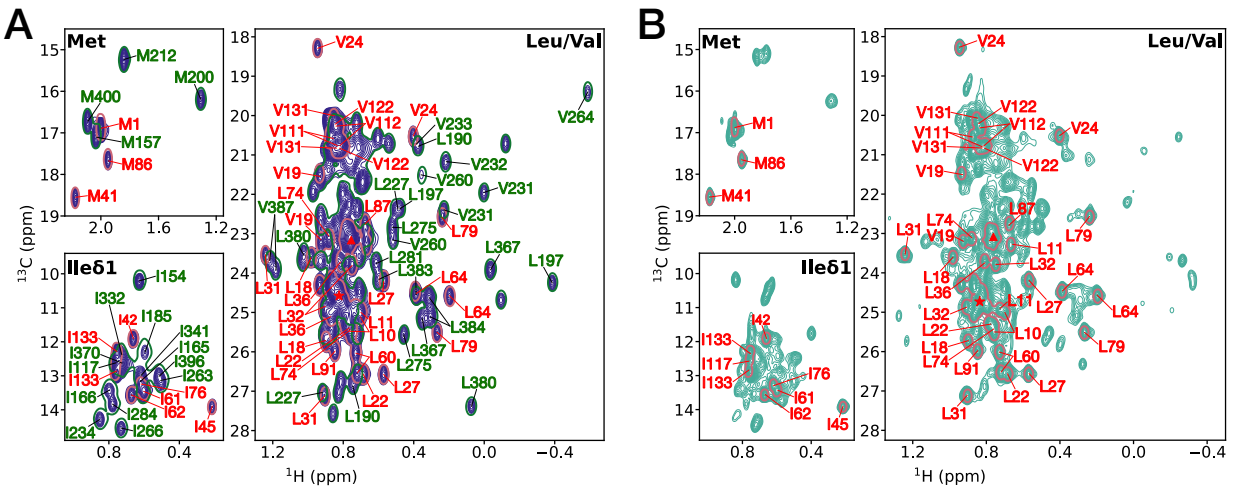

Figure S3. Individual Casp9 domains from the full-length construct behave independently. (**A**) 2D ^{1}H-^{13}C HMQC spectra (800 MHz, 25°C) of U-^{2}H, ILVM-labeled WT Casp9 FL (navy contours), WT Casp9 PD (green single contours), and Casp9 CARD+linker (pink single contours) showing that crosspeaks from the different constructs superimpose. Assignments of residues in the PD (green labels) and CARD (red labels) are displayed. Triangles (▲) and stars (⋆) indicate positions of CARD residues L11, L91, L100, L105, L108, L113, and L123 and CARD residues L16, L87, L100, L105, L108, L113, and L123, respectively. (**B**) 2D ^{1}H-^{13}C HMQC spectra (800 MHz, 25°C) of U-^{2}H, ILVM-labeled WT Casp9 FL + Z-LEHD-fmk inhibitor (turquoise contours) and Casp9 CARD+linker (pink single contours) illustrating that the spectrum of the CARD+linker does not change upon dimerization of the PD. Only CARD residue assignments are annotated.

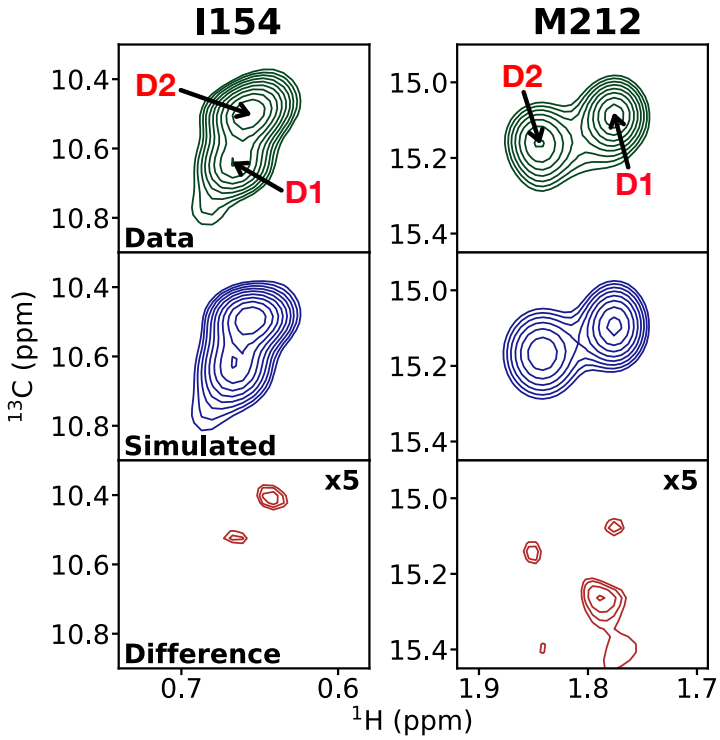

Residue	D2 / D1
I154	1.09 ± 0.01
M212	1.08 ± 0.02

Figure S4. Selected regions of a 2D ^{1}H-^{13}C HMQC spectrum (600 MHz, 25 °C) recorded on a sample of 88 µM U-^{2}H, ILVM-labeled WT Casp9 PD with 400 µM of Z-LEHD-fmk inhibitor, focussing on correlations from residues I154 and M212 (top). As the reaction with the inhibitor has gone to completion, only dimer peaks are present. The D1 and D2 peaks (top panels) were fit to Gaussian lineshapes to generate simulated peaks (middle panels). The difference between experimental and simulated peaks (bottom panels) are plotted at 5-fold lower contour levels, illustrating the good fit. The ratios of extracted peak volumes, D2/D1, are indicated (bottom). See "*Effect of assumption of equal volumes for I154 and M212 dimer peaks, D1=D2* (Fig. 3B and Fig. 6)" for further discussion.

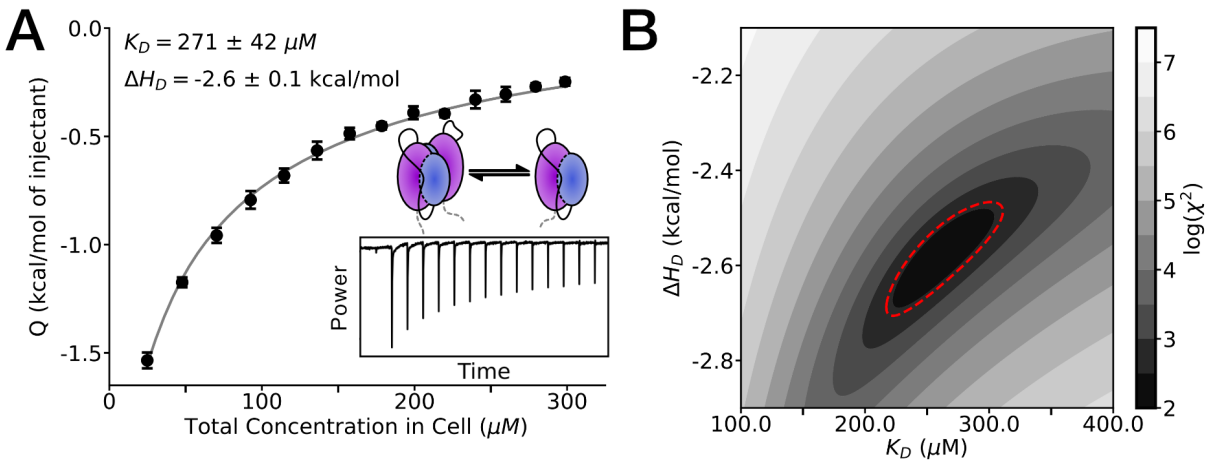

Figure S5. (A) ITC profile of C287A Casp9 PD at 25°C. The experimental heats (black circles) were fit (solid line) to a monomer-dimer dissociation model ($M + M \rightleftharpoons M_2$), and K_D and ΔH_D values were extracted. A raw thermogram is shown in the inset. (B) A chi-squared (χ^2) surface plot was constructed (as described in *SI Appendix*, Fig. S2) in order to assess the correlations between parameters. Values at the 95% confidence level (dotted red lines) are consistent with those obtained from triplicate measurements.

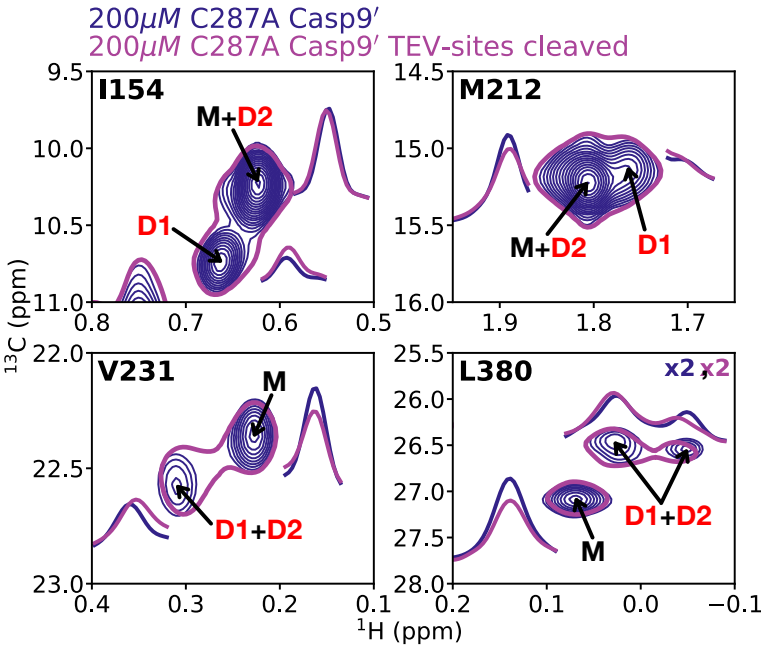

Figure S6. Superposition of selected regions of 2D ^{1}H-^{13}C HMQC spectra (800 MHz, 25°C) recorded on samples of 200 μM U-^{2}H, ILVM-labeled C287A Casp9′ (navy contours) and C287A Casp9′ with the TEV-sites in the p20-p10 linker cleaved (pink single contours). The traces adjacent to the peaks are box-sums over the following ^{13}C chemical shift ranges: I154 M+D2, 9.9-10.4 ppm; I154 D1, 10.5-11.0 ppm; M212 M+D2, 15.0-15.4 ppm; M212 D1, 14.9-15.3 ppm; V231 M, 22.2-22.6 ppm; V231 D1+D2, 22.4-22.8 ppm; L380 M, 26.9-27.4 ppm; L380 D1&D2, 26.2-26.7 ppm. A comparison of 1D box-sum profiles of monomer (M) and dimer (D) peaks for the two constructs makes it clear that there is only a minimal change in the monomer-dimer equilibrium between C287A Casp9′ with an intact linker connecting the p10 and p20 domains and a 'TEV-sites construct of C287A Casp9′' where a pair of sites that are auto-proteolyzed by the WT enzyme (E306, D315) (32) are cleaved using TEV-protease.

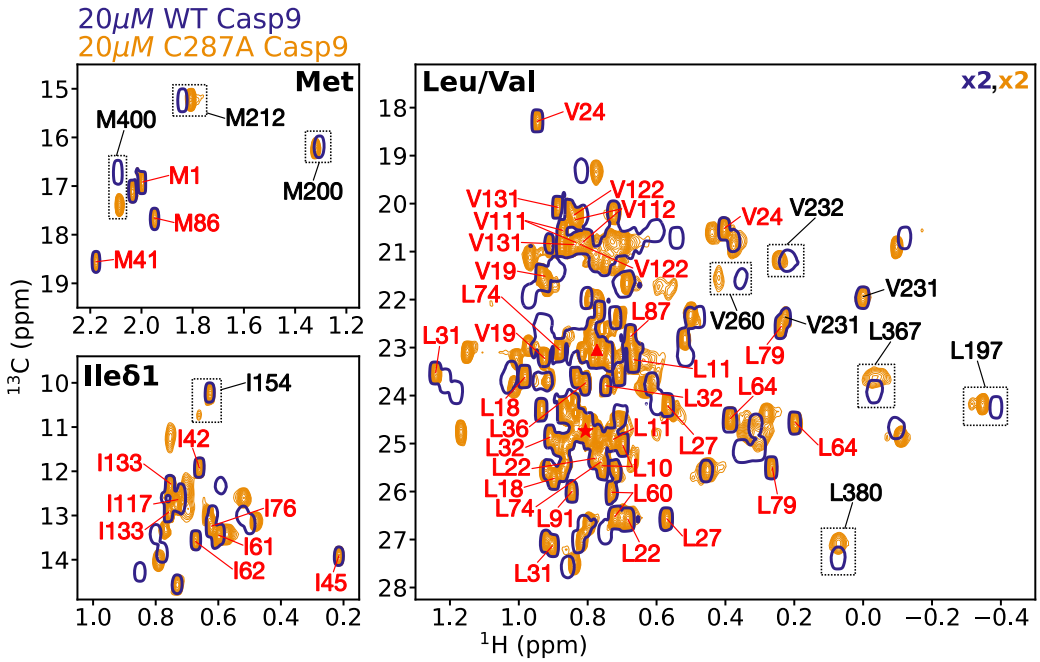

Figure S7. Overlay of 2D ^{1}H-^{13}C HMQC spectra (1GHz, 25°C) recorded on 20 μM U-^{2}H, ILVM samples of WT Casp9 FL (navy single contours) and C287A Casp9 FL (orange contours). A total protein concentration of 20 μM was chosen as there is only minimal dimerization for the C287A construct at this concentration. Significant chemical shift changes are seen between the two spectra, illustrating the perturbing effect of the C287A mutation in the Casp9 PD. Note that these shift changes are not restricted to regions proximal to the site of mutation; for example the closest distances between pairs of atoms of C287 and M212 or L380 are 12.7 Å and 19.4 Å, respectively. Select crosspeaks derived from PD (black) and all crosspeaks from CARD (red, see *SI Appendix*, Fig. S3 legend for ▲ and ⋆ assignments) are annotated, demonstrating that the perturbing effect is localized to the PD.

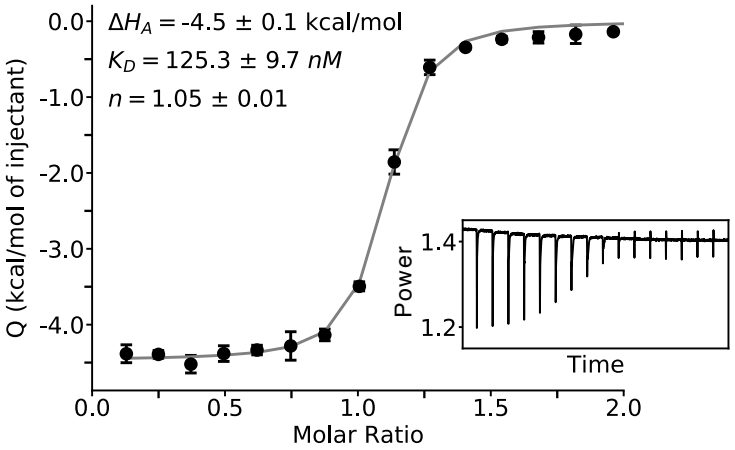

Figure S8. ITC profile of the binding of the Ark1p peptide (syringe) to Abp1p-SH3 (cell) at 25°C. The experimental heats (black circles) were fit (solid line) to an *n*-sites non-cooperative protein+ligand model ($P + nL \rightleftharpoons PL_n$), and ΔH_A, K_D and n values were extracted. A raw thermogram is shown in the inset.

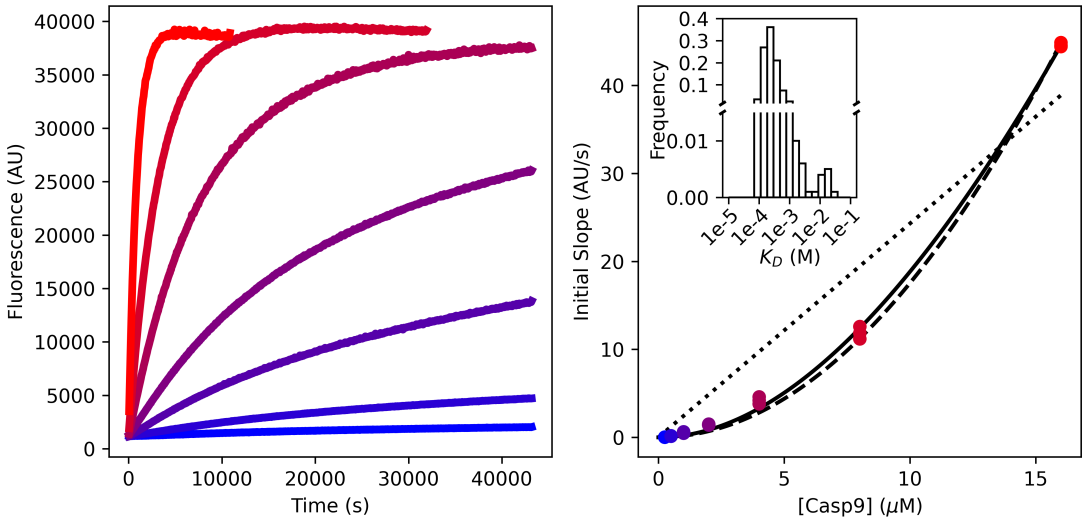

Figure S9. Concentration dependence of Casp9 activity monitored by the increase in fluorescence upon cleavage of Ac-LEHD-AMC. (A) Fluorescence timecourse as a function of the total Casp9 concentration, ranging from 0.25 μM (blue) to 16 μM (red). (B) The fitted initial rates (colored circles; in triplicates), obtained from analysis of the linear portions of the timecourse data (only one of the three timecourses is shown on the left), are plotted vs the total Casp9 concentration, showing a dependence which is well-approximated by a quadratic (solid curve) rather than a linear (dotted line) function, as would be expected for a Casp9 activity profile that depends on the concentration of dimer and for which the dimer dissociation constant is much larger than the total Casp9 concentration (i.e., rate $\propto$ [D] $\propto$ $[M]^2 \approx [M_T]^2$ when $K_D >>$ [M], where [D], [M], and $[M_T]$ are the concentrations of dimer, monomer, and total Casp9 protein, respectively, and K_D is the dimer dissociation constant. Fitting the data to a model in which the Casp9 activity is assumed to be proportional to the amount of dimer yields the dashed curve and K_D = 200 μM (fit to the average of the triplicates). The inset shows the distribution of fitted K_D values based on 1000 Monte Carlo simulations. A strong correlation between dimer formation and enhanced activity have also been observed in previous studies (27, 33).

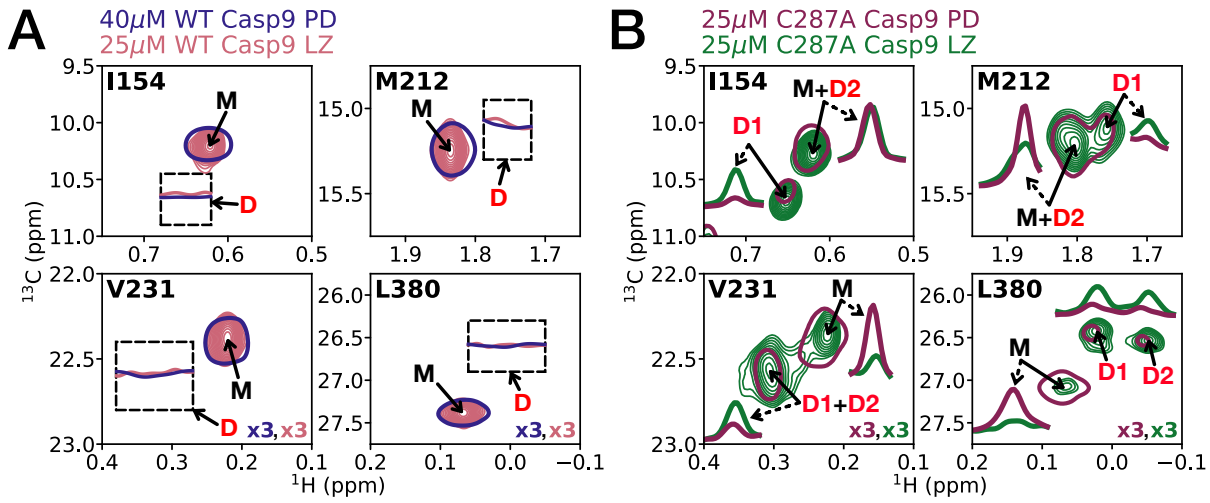

Figure S10. (A) Superposition of selected regions of 2D ^{1}H-^{13}C HMQC spectra recorded on samples of U-^{2}H, ILVM-labeled 40 μM WT Casp9 PD (navy single contours) and 25 μM WT Casp9 LZ (pink contours). Only monomer (M) peaks are observed, with the expected positions of the dimer (D) peaks highlighted by dashed boxes, along with 1D box-sum traces corresponding to sums in the ^{13}C dimension in the boxed regions indicated, illustrating that dimer peaks are not observed. (B) Selected regions of 2D ^{1}H-^{13}C HMQC spectra of U-^{2}H, ILVM-labeled 25 μM C287A Casp9 PD (maroon single contours) and 25 μM C287A Casp9 LZ (green contours). The traces adjacent to the peaks are box-sums over the following ^{13}C chemical shift ranges: I154 M+D2, 9.9-10.4 ppm; I154 D1, 10.5-11.0 ppm; M212 M+D2, 15.0-15.4 ppm; M212 D1, 14.9-15.3 ppm; V231 M, 22.2-22.6 ppm; V231 D1+D2, 22.4-22.8 ppm; L380 M, 26.9-27.4 ppm; L380 D1&D2, 26.2-26.7 ppm. These 1D box-sum traces highlight that monomer (dimer) peak volumes decrease (increase) when two C287A PDs are tethered via the leucine zipper dimer motif relative to untethered C287A PDs. Dashed arrows link box-sums with the corresponding crosspeaks.

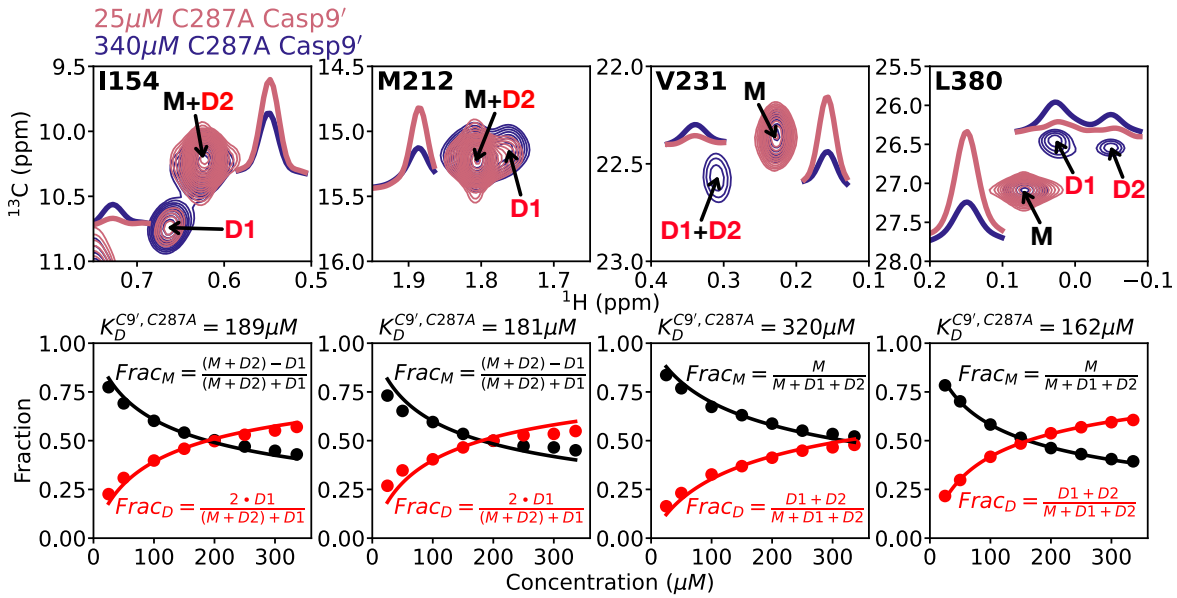

Figure S11. Peak volume changes as a function of protein concentration are observed for monomer-dimer crosspeaks of selected residues in 2D ^{1}H-^{13}C HMQC spectra of U-^{2}H, ILVM-labeled C287A Casp9′ (top panels), 800 MHz, 25 ºC. The 1D-traces of the box-sums for each crosspeak are shown adjacent to the peak in question and are summed over the following ^{13}C chemical shift ranges: I154 M+D2, 9.9-10.4 ppm; I154 D1, 10.5-11.0 ppm; M212 M+D2, 15.0-15.4 ppm; V231 M, 22.2-22.6 ppm; V231 D1+D2, 22.4-22.8 ppm; L380 M, 26.9-27.4 ppm; L380 D1&D2, 26.2-26.7 ppm. The monomer population decreases with increasing protein concentration, as observed in a comparison of spectra recorded at concentrations of 25 μM (pink contours) and 340 μM (navy contours). For I154 and M212 one dimer peak (arbitrarily assigned as D2) overlaps with the monomer (M) correlation, while for V231 and L380 the two dimer peaks are distinct from the monomer peak. The fraction monomer (black circles) and dimer (red circles) as a function of concentration are plotted and fit (solid lines) on a per residue basis (bottom panels) to extract the dissociation constants shown, yielding an average value of 213 ± 72 μM.

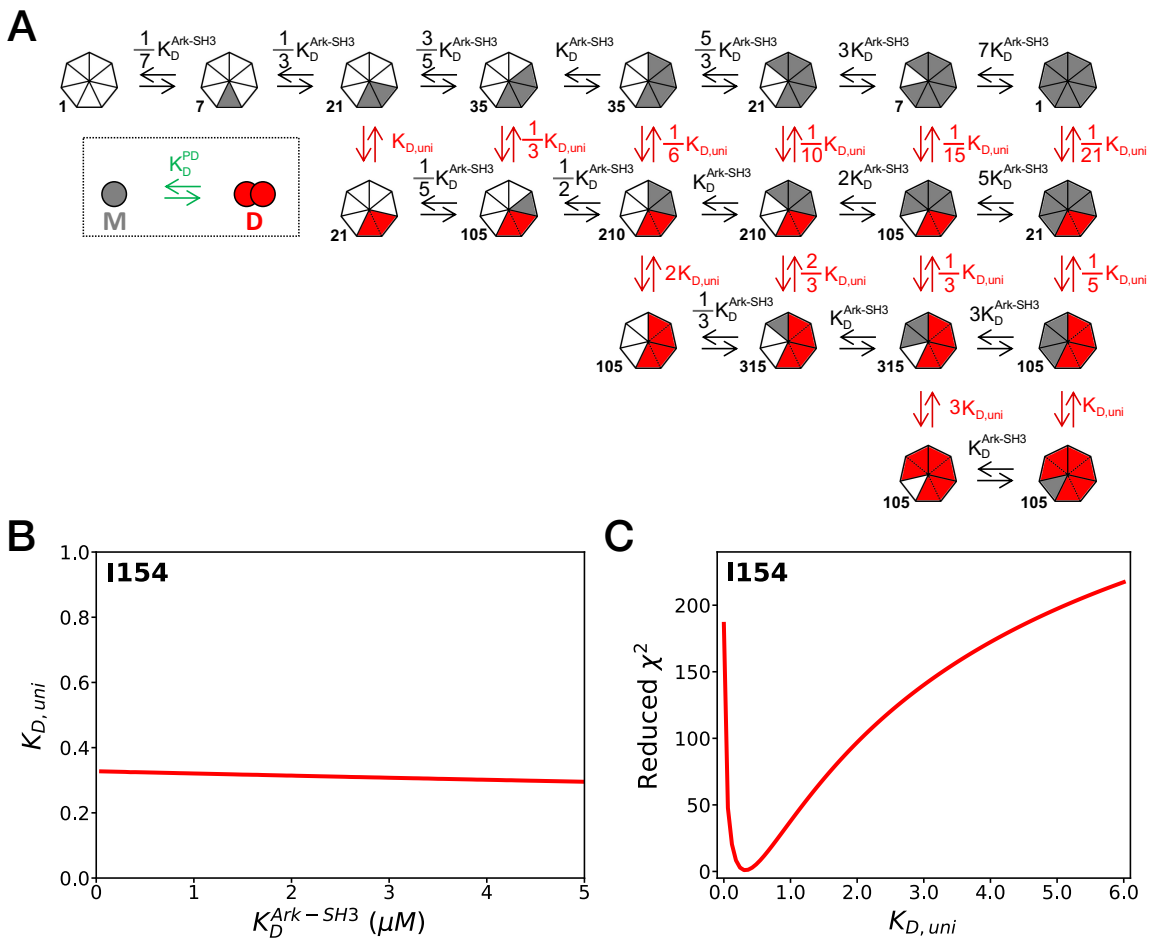

Figure S12. (A) Thermodynamic scheme used to model the titration of $Casp9'$ with α'_7. The heptameric structure of α'_7 is depicted as a heptagon comprised of seven triangles each representing a single α' protomer. White, grey, and red triangles denote α' protomers that are unbound, bound with monomeric $Casp9'$, or bound with $Casp9'$ that is part of a dimer due to PD interactions between $Casp9'$ molecules on the same α'_7 scaffold. $K_D^{Ark-SH3}$ and $K_{D,uni}$ refer to the microscopic bimolecular and unimolecular dissociations constants for the $Casp9'$ - α' interaction, and the coefficients associated with them take into accout the number of ways that $Casp9'$ can bind to, or be removed from, the scaffold. Each number on the left bottom edge of a heptagon indicates the degeneracy of that state. This can be calculated as degeneracy =

$\binom{7}{n_Y + n_Z}\binom{n_Y + n_Z}{n_Z}\frac{n_Z!}{2^{n_Z/2}\cdot(n_Z/2)!}$, where n_Y and n_Z are the number of $Casp9'$ molecules bound to α_7' as monomers or dimers, respectively, (in total n_Y + n_Z molecules are bound) and $\binom{a}{b} = \frac{a!}{(a-b)!b!}$. For example, for the case where 5 monomers of $Casp9'$ are bound, degeneracy = $\binom{7}{5}\binom{5}{0}\frac{0!}{2^0\cdot\left(\frac{0}{2}\right)!} = 21$. In the general case the degeneracy is given by the number of ways of arranging n_Y + n_Z bound molecules on α_7' (first term) multiplied by the number of ways choosing from the n_Y + n_Z bound molecules the n_Z molecules that will be dimerizing (second term) multiplied by the number of ways of creating unique dimeric pairs from these n_Z molecules (third term). The third term is slightly more complex than the first two but can be rationalized by realizing that it can be calculated from $\binom{n_z}{2}\binom{n_z-2}{2}\binom{n_z-4}{2}\ldots 1 = \frac{n_z!}{2^{n_z/2}}$, which is the product of the number of ways of selecting the first two $Casp9'$ molecules for dimerization with the number of ways of selecting the next two $Casp9'$ molecules and so on, until all the n_z molecules are dimerized. However, this procedure overcounts the number of ways by $\left(\frac{n_z}{2}\right)!$ because the order that the $\frac{n_z}{2}$ pairs of $Casp9'$ molecules are selected is irrelevant in this case. (B) Plot of $K_{D,uni}$ (residue I154) as a function of $K_D^{Ark-SH3}$, demonstrating a minimal effect of $K_D^{Ark-SH3}$ on the fitted value of $K_{D,uni}$. (C) 1D plot of χ^2_{red} vs $K_{D,uni}$ for the titration profile of I154 (Fig. 5C), with $K_D^{Ark-SH3}$ set to the measured value of 0.55 μM. The value of χ^2_{red} is defined as $\chi^2_{red} = \sum\frac{(Exp-Cal)^2}{\sigma^2}$, where σ is obtained from the average deviation between the experimental points (*Exp*) and the best fit calculated (*Cal*) points. Note that I154 was chosen arbitrarily, and the $K_{D,uni}$ values for all fitted residues are similarly well defined.

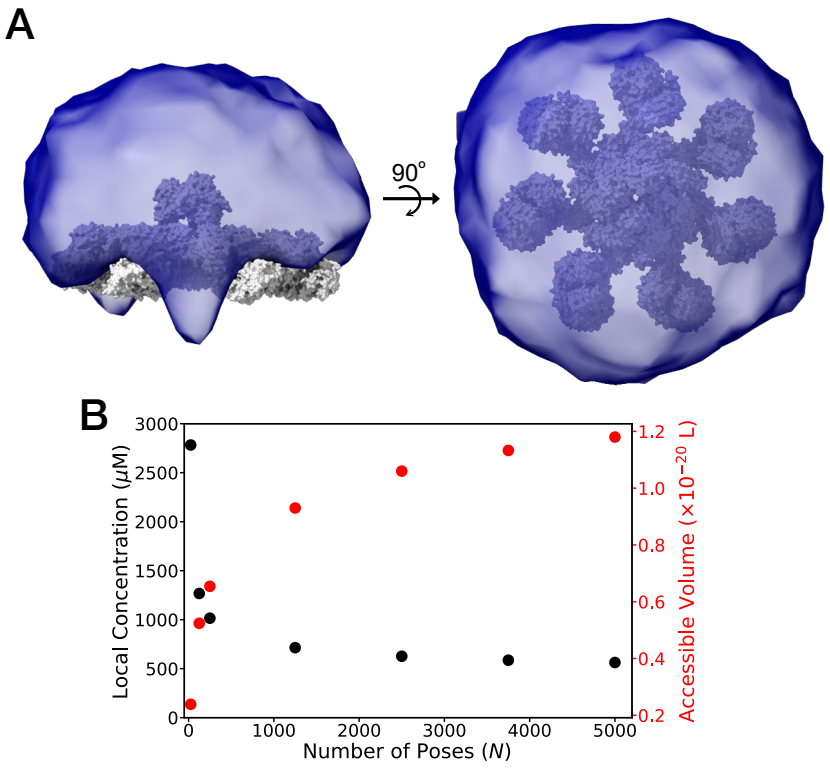

Figure S13. *In silico* modeling of the local Casp9 PD concentration on the apoptosome. (A) The transparent blue surface represents the total volume (*N*=5000 poses) that is accessible to the Casp9 PDs when bound to the apoptosome (PDB ID: 5WVE (11), grey) via $CARD_{Casp9}$:$CARD_{Apaf1}$ interactions. (B) Local concentration of Casp9 PDs calculated assuming four bound Casp9 molecules (*SI Appendix*). The local concentration (total accessible volume) plateaus at a value of approximately 560 μM (1.18×10^{-20} L).

Table S1. Amino acid sequences and extinction coefficients of constructs.

Construct Name	Amino Acid Sequence	Extinction Coefficient ($\varepsilon_{280,\ M^{-1}cm^{-1}}$)
Casp9	SGMDEADRRLLRRCRLRLVEELQVDQLWDALLSRELFRPHMIEDIQRAGSGSRRDQARQLII DLETRGSQALPLFISCLEDTGQDMLASFLRTNRQAAKLSKPTLENLTPVVLRPEIRKPEVLR PETPRPVDIGSGGFGDVGALESLRGNADLAYILSMEPCGHCLIINNVNFCRESGLRTRTGSN IDCEKLRRRFSSLHFMVEVKGDLTAKKMVLALLELAQQDHGALDCCVVVILSHGCQASHLQF PGAVYGTDGCPVSVEKIVNIFNGTSCPSLGGKPKLFFIQACGGEQKDHGFEVASTSPEDESP GSNPEPDATPFQEGLRTFDQLDAISSLPTPSDIFVSYSTFPGFVSWRDPKSGSWYVETLDDI FEQWAHSEDLQSLLLRVANAVSVKGIYKQMPGCFNFLRKKLFFKTS	29,450
Casp9 PD	SGGALESLRGNADLAYILSMEPCGHCLIINNVNFCRESGLRTRTGSNIDCEKLRRRFSSLHF MVEVKGDLTAKKMVLALLELAQQDHGALDCCVVVILSHGCQASHLQFPGAVYGTDGCPVSVE KIVNIFNGTSCPSLGGKPKLFFIQACGGEQKDHGFEVASTSPEDESPGSNPEPDATPFQEGL RTFDQLDAISSLPTPSDIFVSYSTFPGFVSWRDPKSGSWYVETLDDIFEQWAHSEDLQSLLL RVANAVSVKGIYKQMPGCFNFLRKKLFFKTS	23,950
C9toC3	SGGALESLRGNADLAYILSMEPCGHCLIINNVNFCRESGLRTRTGSNIDCEKLRRRFSSLHF MVEVKGDLTAKKMVLALLELAQQDHGALDCCVVVILSHGCQASHLQFPGAVYGTDGCPVSVE KIVNIFNGTSCPSLGGKPKLFFIQACGGEQKDHGFEVASTSPEDESPGSNPEPDATPFQEGL RTFDQLDAISSLPTPSDIFVSYSTFPGFVSWRDPKSGSWYVETLDDIFEQWAHSEDLQSLLL RVANAVSVKGIYKQMPCIVSMLRKKLFFKTS	23,950
Casp9 CARD+linker	SGMDEADRRLLRRCRLRLVEELQVDQLWDALLSRELFRPHMIEDIQRAGSGSRRDQARQLII DLETRGSQALPLFISCLEDTGQDMLASFLRTNRQAAKLSKPTLENLTPVVLRPEIRKPEVLR PETPRPVDIGSGGFGD	5,500
Casp9′	SAMAPWATAEYDYDAAEDNELTFVENDKIINIEFVDDDWWLGELEKDGSKGLFPSNYVSLGN AKLSKPTLENLTPVVLRPEIRKPEVLGFEVKKSVDIGSGGFGDVGALESLRGNADLAYILSM EPCGHCLIINNVNFCRESGLRTRTGSNIDCEKLRRRFSSLHFMVEVKGDLTAKKMVLALLEL AQQDHGALDCCVVVILSHGCQASHLQFPGAVYGTDGCPVSVEKIVNIFNGTSCPSLGGKPKL FFIQACGGEQKDHGFEVASTSPEDESPGSNPEPDATPFQEGLRTFDQLDAISSLPTPSDIFV SYSTFPGFVSWRDPKSGSWYVETLDDIFEQWAHSEDLQSLLLRVANAVSVKGIYKQMPGCFN FLRKKLFFKTS	44,920
Casp9 LZ	SGKQLEDKVEELLSKNYHLENEVARLKKLVGERAKLSKPTLENLTPVVLRPEIRKPEVLRPE TPRPVDIGSGGFGDVGALESLRGNADLAYILSMEPCGHCLIINNVNFCRESGLRTRTGSNID CEKLRRRFSSLHFMVEVKGDLTAKKMVLALLELAQQDHGALDCCVVVILSHGCQASHLQFPG AVYGTDGCPVSVEKIVNIFNGTSCPSLGGKPKLFFIQACGGEQKDHGFEVASTSPEDESPGS NPEPDATPFQEGLRTFDQLDAISSLPTPSDIFVSYSTFPGFVSWRDPKSGSWYVETLDDIFE QWAHSEDLQSLLLRVANAVSVKGIYKQMPGCFNFLRKKLFFKTS	25,440
α′	KKTKPTPPPKPSHLKPKGIPVVSSSSGKDSVSGTVFSPDGRLFQVEYAREAVKKGSTALGMK FANGVLLISDKKVRSRLIEQNSIEKIQLIDDYVAAVTSGLVADARVLVDFARISAGSLVNIE NLVKRVADQMQQYTQYGGVRPYGVSLIFAGIDQIGPRLFDCDPAGTINEYKATAIGSGKDAV VSFLEREYKENLPEKEAVTLGIKALKSSLEEGEELKAPEIASITVGNKYRIYDQEEVKKFL	13,410
C287A Casp9′ TEV-sites in p20-p10 linker	SAMAPWATAEYDYDAAEDNELTFVENDKIINIEFVDDDWWLGELEKDGSKGLFPSNYVSLGN AKLSKPTLENLTPVVLRPEIRKPEVLGFEVKKSVDIGSGGFGDVGALESLRGNADLAYILSM EPCGHCLIINNVNFCRESGLRTRTGSNIDCEKLRRRFSSLHFMVEVKGDLTAKKMVLALLEL AQQDHGALDCCVVVILSHGCQASHLQFPGAVYGTDGCPVSVEKIVNIFNGTSCPSLGGKPKL FFIQAAGGEQKDHGFEVASENLYFQSPGENLYFQATPFQEGLRTFDQLDAISSLPTPSDIFV SYSTFPGFVSWRDPKSGSWYVETLDDIFEQWAHSEDLQSLLLRVANAVSVKGIYKQMPGCFN FLRKKLFFKTS	47,900
Apaf1	MDAKARNCLLQHREALEKDIKTSYIMDHMISDGFLTISEEEKVRNEPTQQQRAAMLIKMILK KDNDSYVSFYNALLHEGYKDLAALLHDGIPVVSSSSGKDSVSGITSYVRTVLCEGGVPQRPV VFVTRKKLVNAIQQKLSKLKGEPGWVTIHGMAGCGKSVLAAEAVRDHSLLEGCFPGGVHWVS VGKQDKSGLLMKLQNLCTRLDQDESFSQRLPLNIEEAKDRLRILMLRKHPRSLLILDDVWDS WVLKAFDSQCQILLTTRDKSVTDSVMGPKYVVPVESSLGKEKGLEILSLFVNMKKADLPEQA HSIIKECKGSPLVVSLIGALLRDFPNRWEYYLKQLQNKQFKRIRKSSSYDYEALDEAMSISV EMLREDIKDYYTDLSILQKDVKVPTKVLCILWDMETEEVEDILQEFVNKSLLFCDRNGKSFR YYLHDLQVDFLTEKNCSQLQDLHKKIITQFQRYHQPHTLSPDQEDCMYWYNFLAYHMASAKM HKELCALMFSLDWIKAKTELVGPAHLIHEFVEYRHILDEKDCAVSENFQEFLSLNGHLLGRQ PFPNIVQLGLCEPETSEVYQQAKLQAKQEVDNGMLYLEWINKKNITNLSRLVVRPHTDAVYH	189,190

	ACFSEDGQRIASCGADKTLQVFKAETGEKLLEIKAHEDEVLCCAFSTDDRFIATCSVDKKVK IWNSMTGELVHTYDEHSEQVNCCHFTNSSHHLLLATGSSDCFLKLWDLNQKECRNTMFGHTN SVNHCRFSPDDKLLASCSADGTLKLWDATSANERKSINVKQFFLNLEDPQEDMEVIVKCCSW SADGARIMVAAKNKIFLFDIHTSGLLGEIHTGHHSTIQYCDFSPQNHLAVVALSQYCVELWN TDSRSKVADCRGHLSWVHGVMFSPDGSSFLTSSDDQTIRLWETKKVCKNSAVMLKQEVDVVF QENEVMVLAVDHIRRLQLINGRTGQIDYLTEAQVSCCCLSPHLQYIAFGDENGAIEILELVN NRIFQSRFQHKKTVWHIQFTADEKTLISSSDDAEIQVWNWQLDKCIFLRGHQETVKDFRLLK NSRLLSWSFDGTVKVWNIITGNKEKDFVCHQGTVLSCDISHDATKFSSTSADKTAKIWSFDL LLPLHELRGHNGCVRCSAFSVDSTLLATGDDNGEIRIWNVSNGELLHLCAPLSEEGAATHGG WVTDLCFSPDGKMLISAGGYIKWWNVVTGESSQTFYTNGTNLKKIHVSPDFKTYVTVDNLGI LYILQTLEHHHHHHHHH	
Ark1p Peptide	GAMAKKTKPTPPPKPSHLKPK	N/A
Abp1p-SH3	GAMAPWATAEYDYDAAEDNELTFVENDKIINIEFVDDDWWLGELEKDGSKGLFPSNYVSLGN	20,970

References

1. R. D. Grinshpon, A. Williford, J. Titus-McQuillan, A. Clay Clark, The CaspBase: a curated database for evolutionary biochemical studies of caspase functional divergence and ancestral sequence inference: Tools for Caspase Sequence Analysis and Evolutionary Biochemistry. *Protein Sci.* **27**, 1857–1870 (2018).

2. R. Sprangers, *et al.*, TROSY-Based NMR Evidence for a Novel Class of 20S Proteasome Inhibitors. *Biochemistry* **47**, 6727–6734 (2008).

3. Q. Yin, *et al.*, Caspase-9 Holoenzyme Is a Specific and Optimal Procaspase-3 Processing Machine. *Mol. Cell* **22**, 259–268 (2006).

4. P. Vallurupalli, D. F. Hansen, E. Stollar, E. Meirovitch, L. E. Kay, Measurement of bond vector orientations in invisible excited states of proteins. *Proc. Natl. Acad. Sci.* **104**, 18473–18477 (2007).

5. V. Tugarinov, L. E. Kay, An Isotope Labeling Strategy for Methyl TROSY Spectroscopy. *J. Biomol. NMR* **28**, 165–172 (2004).

6. I. Gelis, *et al.*, Structural Basis for Signal-Sequence Recognition by the Translocase Motor SecA as Determined by NMR. *Cell* **131**, 756–769 (2007).

7. L. Siemons, H. W. Mackenzie, V. K. Shukla, D. F. Hansen, Intra-residue methyl–methyl correlations for valine and leucine residues in large proteins from a 3D-HMBC-HMQC experiment. *J. Biomol. NMR* **73**, 749–757 (2019).

8. M. P. Malakhov, *et al.*, SUMO fusions and SUMO-specific protease for efficient expression and purification of proteins. *J. Struct. Funct. Genomics* **5**, 75–86 (2004).

9. V. A. Luckow, S. C. Lee, G. F. Barry, P. O. Olins, Efficient generation of infectious recombinant baculoviruses by site-specific transposon-mediated insertion of foreign genes into a baculovirus genome propagated in *Escherichia coli*. *J. Virol.* **67**, 4566–4579 (1993).

10. T. C. Cheng, C. Hong, I. V. Akey, S. Yuan, C. W. Akey, A near atomic structure of the active human apoptosome. *eLife* **5**, e17755 (2016).

11. Y. Li, *et al.*, Mechanistic insights into caspase-9 activation by the structure of the apoptosome holoenzyme. *Proc. Natl. Acad. Sci.* **114**, 1542–1547 (2017).

12. M. Guo, B. Bhaskar, H. Li, T. P. Barrows, T. L. Poulos, Crystal structure and characterization of a cytochrome c peroxidase–cytochrome c site-specific cross-link. *Proc. Natl. Acad. Sci.* **101**, 5940–5945 (2004).

13. B. A. Callus, D. L. Vaux, Caspase inhibitors: viral, cellular and chemical. *Cell Death Differ.* **14**, 73–78 (2007).

14. N. A. Pereira, Z. Song, Some commonly used caspase substrates and inhibitors lack the specificity required to monitor individual caspase activity. *Biochem. Biophys. Res. Commun.* **377**, 873–877 (2008).

15. A. Velazquez-Campoy, S. A. Leavitt, E. Freire, "Characterization of Protein–Protein Interactions by Isothermal Titration Calorimetry" in *Protein-Protein Interactions*, H. Fu, Ed. (Humana Press, 2004), pp. 183–204.

16. F. Delaglio, *et al.*, NMRPipe: A multidimensional spectral processing system based on UNIX pipes. *J. Biomol. NMR* **6** (1995).

17. M. Sattler, C. Griesinger, J. Schleucher, Heteronuclear multidimensional NMR experiments for the structure determination of proteins in solution employing pulsed field gradients. *Prog. Nucl. Magn. Reson. Spectrosc.* **34**, 93–158 (1999).

18. S. C. Panchal, N. S. Bhavesh, R. V. Hosur, Improved 3D triple resonance experiments, HNN and HN(C)N, for H^N and ^{15}N sequential correlations in (^{13}C, ^{15}N) labeled proteins: Application to unfolded proteins. *J. Biomol. NMR* **20**, 135–147 (2001).

19. A. Bax, D. Max, D. Zax, Measurement of long-range ^{13}C-^{13}C J couplings in a 20-kDa protein-peptide complex. *J. Am. Chem. Soc.* **114**, 6923–6925 (1992).

20. S. G. Hyberts, K. Takeuchi, G. Wagner, Poisson-Gap Sampling and Forward Maximum Entropy Reconstruction for Enhancing the Resolution and Sensitivity of Protein NMR Data. *J. Am. Chem. Soc.* **132**, 2145–2147 (2010).

21. J. Ying, F. Delaglio, D. A. Torchia, A. Bax, Sparse multidimensional iterative lineshape-enhanced (SMILE) reconstruction of both non-uniformly sampled and conventional NMR data. *J. Biomol. NMR* **68**, 101–118 (2017).

22. J. Jumper, *et al.*, Highly accurate protein structure prediction with AlphaFold. *Nature* **596**, 583–589 (2021).

23. M. Varadi, *et al.*, AlphaFold Protein Structure Database: massively expanding the structural coverage of protein-sequence space with high-accuracy models. *Nucleic Acids Res.* **50**, D439–D444 (2022).

24. M. Renatus, H. R. Stennicke, F. L. Scott, R. C. Liddington, G. S. Salvesen, Dimer formation drives the activation of the cell death protease caspase 9. *Proc. Natl. Acad. Sci.* **98**, 14250–14255 (2001).

25. Y. Chao, *et al.*, Engineering a Dimeric Caspase-9: A Re-evaluation of the Induced Proximity Model for Caspase Activation. *PLoS Biol.* **3**, e183 (2005).

26. E. N. Shiozaki, *et al.*, Mechanism of XIAP-Mediated Inhibition of Caspase-9. *Mol. Cell* **11**, 519–527 (2003).

27. Q. Hu, *et al.*, Molecular determinants of caspase-9 activation by the Apaf-1 apoptosome. *Proc. Natl. Acad. Sci.* **111**, 16254–16261 (2014).

28. J. M. C. Teixeira, *et al.*, IDPConformerGenerator: A Flexible Software Suite for Sampling the Conformational Space of Disordered Protein States. *J. Phys. Chem. A* **126**, 5985–6003 (2022).

29. Z. H. Liu, *et al.*, “Local Disordered Region Sampling (LDRS) for Ensemble Modeling of Proteins with Experimentally Undetermined or Low Confidence Prediction Segments” BioRxiv [Preprint] (2023) https:/doi.org/10.1101/2023.07.25.550520 (accessed 7 September 2023).

30. T. D. Goddard, *et al.*, UCSF ChimeraX: Meeting modern challenges in visualization and analysis: UCSF ChimeraX Visualization System. *Protein Sci.* **27**, 14–25 (2018).

31. E. F. Pettersen, *et al.*, UCSF ChimeraX: Structure visualization for researchers, educators, and developers. *Protein Sci.* **30**, 70–82 (2021).

32. Q. Hu, D. Wu, W. Chen, Z. Yan, Y. Shi, Proteolytic Processing of the Caspase-9 Zymogen Is Required for Apoptosome-mediated Activation of Caspase-9. *J. Biol. Chem.* **288**, 15142–15147 (2013).

33. H. Roschitzki-Voser, *et al.*, Human caspases in vitro: Expression, purification and kinetic characterization. *Protein Expr. Purif.* **84**, 236–246 (2012).